A new odontocete (toothed cetacean) from the Early Miocene of Peru expands the morphological disparity of extinct heterodont dolphins

Olivier Lambert[a]*, Christian de Muizon[b], Elisa Malinverno[c], Claudio Di Celma[d], Mario Urbina[e] and Giovanni Bianucci[f]

[a]D.O. Terre et Histoire de la Vie, Institut Royal des Sciences Naturelles de Belgique, Brussels, Belgium; [b]CR2P UMR 7207, (MNHN, CNRS, UPMC, Sorbonne-Université), Muséum national d'Histoire naturelle, Département Origines et Évolution, Paris, France; [c]Dipartimento di Scienze dell'Ambiente e della Terra, Università di Milano-Bicocca, Milan, Italy; [d]Scuola di Scienze e Tecnologie, Università di Camerino, Camerino, Italy; [e]Departamento de Paleontología de Vertebrados, Museo de Historia Natural-UNMSM, Lima, Peru; [f]Dipartimento di Scienze della Terra, Università di Pisa, Pisa, Italy

*Corresponding author. Email: olivier.lambert@naturelsciences.be

A key step of the evolutionary history of Odontoceti (echolocating toothed cetaceans) is the transition from the ancestral heterodont condition - characterized by the presence of double-rooted cheek teeth bearing accessory denticles - to the homodont dentition displayed by most extant odontocete species. During the last decades, new finds and the reassessment of specimens in collections revealed an increased morphological disparity among the Oligo-Miocene heterodont odontocetes. Based on a partly articulated skeleton from late Early Miocene (Burdigalian, 18.8-18.0 Ma) beds of the Chilcatay Formation (Pisco Basin, Peru), we describe a new genus and species of heterodont odontocete, *Inticetus vertizi*, in the new family Inticetidae. This large dolphin is characterized, among others, by: a long and robust rostrum bearing at least 18 teeth per quadrant; the absence of procumbent anterior teeth; many large, broad-based accessory denticles in double-rooted posterior cheek teeth; a reduced ornament of dental crowns; the styliform process of the jugal being markedly robust; a large fovea epitubaria on the periotic, with a correspondingly voluminous accessory ossicle of the tympanic bulla; and a shortened tuberculum of the malleus.

Phylogenetic analyses (with and without molecular constraint, with and without down-weighting of homoplastic characters) yielded contrasting results, with *Inticetus* falling either as a stem Odontoceti or as an early branching member of a large Platanistoidea clade.

With its large size, robust rostrum, unusual dental morphology, and the absence of conspicuous tooth wear, *Inticetus* increases the morphological and ecological disparity of Late Oligocene - Early Miocene heterodont odontocetes. Finally, this new taxon calls for caution when attempting to identify isolated cetacean cheek teeth, even at the suborder level.

http://zoobank.org/urn:lsid:zoobank.org:pub:5B306B49-EB1B-42F9-B755-B0B05B4F938F

Keywords: Cetacea; Odontoceti; heterodont; Miocene; Burdigalian; Peru

Introduction

Most modern odontocetes (echolocating toothed cetaceans) are characterized by a roughly homodont and polydont dentition, resulting from the progressive simplification and multiplication of the teeth of their ancestors, in relation with major changes in predation techniques and food processing (Fordyce 1982; Uhen 2009; Armfield *et al.* 2013).

Nevertheless, many Oligocene and Miocene odontocetes retain the plesiomorphic condition of double-rooted cheek teeth bearing accessory denticles. For a long time fragmentary fossil specimens displaying various degrees of heterodonty were generally referred to the waste-basket family Squalodontidae, often in the genus *Squalodon* (Fordyce & Muizon 2001; Marx *et al.* 2016; see for example the Paleobiology Database section on *Squalodon*, mostly compiled by M. D. Uhen, mentioning 23 species in the genus). The discovery and description of better-preserved specimens lead to the recognition of several other families, highlighting a high morphological disparity and a complex evolutionary transition to crown odontocetes. Heterodont odontocetes are now distributed in at least seven families: Agorophiidae, Ashleycetidae, Patriocetidae, Simocetidae, Squalodontidae, Waipatiidae, and Xenorophidae (see Whitmore & Sanders 1977; Fordyce 1981, 1994, 2002; Muizon 1991; Uhen 2008b; Geisler *et al.* 2014; Sanders & Geisler 2015; Godfrey *et al.* 2016). Among them, only Squalodontidae and Waipatiidae have been identified as members of the crown Odontoceti clade, in the superfamily Platanistoidea (e.g., Muizon 1991, 1994; Fordyce 1994; Tanaka & Fordyce 2016). However, such attributions did not yet reach a consensus (see Geisler *et al.* 2011; Aguirre-Fernández & Fordyce 2014; Tanaka & Fordyce 2014; Sanders & Geisler 2015; Godfrey *et al.* 2016). Furthermore, the familial affinities of several genera of heterodont and homodont, Late Oligocene - Early Miocene odontocetes are still debated (e.g., *Neosqualodon*, *Papahu*, *Prosqualodon*, and *Squaloziphius*), some of them even falling among stem Odontoceti in some analyses and among crown Odontoceti in others (e.g., Muizon 1991; Fordyce 1994; Geisler *et al.* 2011; Aguirre-Fernández & Fordyce 2014; Godfrey *et al.* 2016; Tanaka & Fordyce 2016; Lambert *et al.* 2017).

In addition to the fossil-rich beds of the late Neogene Pisco Formation, the Pisco Basin, southern coast of Peru, includes older, marine vertebrate-bearing strata ranging from the late Middle Eocene to the earliest Middle Miocene (Muizon & DeVries 1985; Dunbar *et al.* 1990; DeVries 1998; Bianucci *et al.* 2016a). Dated from the latest Oligocene - earliest Middle Miocene, the Chilcatay Formation already yielded the remains of several homodont odontocetes (including kentriodontid-like delphinidans, physeteroids, at least two squalodelphinids, and a member of an unnamed new family), in a relatively poorly constrained stratigraphic context (Lambert *et al.* 2014, 2015; Bianucci *et al.* 2015). Some years ago, the new fossil locality of Roca Negra was discovered in the southern part of the basin, displaying vast outcrops of the Chilcatay Formation. Based on an articulated cetacean skeleton, including the cranium with ear bones, mandibles, teeth, sternum, vertebrae, and ribs, discovered in late Early Miocene (Burdigalian) beds of this locality, we describe a new genus

and species of large heterodont odontocete. We compare the new taxon to other forms from the Oligocene and Early Miocene worldwide, we investigate its phylogenetic relationships, and we discuss the impact of this new genus and species on our understanding of the stem-crown Odontoceti transition.

Material and methods

Institutional abbreviations

MUSM: Museo de Historia Natural, Universidad Nacional Mayor de San Marco, Lima, Peru; **OU:** Geology Museum, University of Otago, Dunedin, New Zealand; **ZMT:** Fossil mammals catalogue, Canterbury Museum, Christchurch, New Zealand.

Anatomical terminology

For cranial anatomical terminology we generally follow Mead & Fordyce (2009) and we mention references when other terms are preferred. The specimen described here being markedly polydont, teeth posterior to canines are named cheek teeth (= C in the text) without any attempt to distinguish between premolars and molars (e.g., Fordyce 1994). The terminology for vertebrae follows Tanaka & Fordyce (2014). Due to the incompleteness of the vertebral column, post-cervical vertebrae are tentatively identified with Roman, instead of Arabic numbers.

Systematic palaeontology

Order **Cetacea** Brisson, 1762

Pelagiceti Uhen, 2008a

Neoceti Fordyce & Muizon, 2001

Suborder **Odontoceti** Flower, 1867

Inticetidae fam. nov.

Type genus. For now, only *Inticetus* gen. nov. is included in the family.

Diagnosis. As for the only included genus.

Inticetus gen. nov.

Type and only included species. *Inticetus vertizi* gen. et sp. nov.

Derivation of name. From *Inti*, the sun deity of the Inca Empire, and *cetus*, whale in Latin, for the typical, subcircular and ray-like arrangement of accessory denticles in posterior cheek teeth of MUSM 1980, reminiscent of artistic reconstructions of the rising sun.

Diagnosis. As for the only included species.

Inticetus vertizi gen. et sp. nov.

(Figs 3-25)

Holotype. MUSM 1980, partial skeleton including the cranium with ear bones, mandibles, teeth, cervical, thoracic, lumbar, and caudal vertebrae, two sternal elements, and ribs. The specimen was discovered by Á. Suárez Vértiz in 2008; the cranium, mandibles, and a few vertebrae were collected by a team lead by M. Urbina in February 2010; A. Altamirano, E. Díaz, G. Bianucci, O. Lambert, C. de Muizon, K. Post, and M. Urbina collected the rest of the skeleton on November 10, 2011.

Type locality. Roca Negra locality, Pisco Basin, 65 km SSE to the city of Ica and 2.4 km west to the Ica River (Fig. 1). Geographic coordinates: S14°39'02.6"-W75°38'53.9"; elevation: 383 m.

Type horizon. The holotype of *Inticetus vertizi* MUSM 1980 was discovered in layers of the Chilcatay Formation, the latter being dated based on diatoms, foraminifers, and molluscs from the latest Oligocene - earliest Middle Miocene (Macharé *et al.* 1988; Dunbar *et al.* 1990; DeVries 1998, 2001). The stratigraphic section of the Roca Negra outcrop is dominated by fine- and medium sandstones with minor amounts of silt and two 0.2 m-thick volcanic ash layers (Fig. 2). By combining data from silicoflagellates (*Naviculopsis ponticula* zone of Bukry 1981) found in a sample located about 5.5 m above MUSM 1980, diatoms from beds containing *N. ponticula spinosa* in another section of the Chilcatay Formation in the Pisco Basin (Pampa Chilcatay; Macharé *et al.* 1998), and the $^{40}Ar/^{39}Ar$ dating of an ash layer just

below the erosional contact of the Chilcatay Formation with the Pisco Formation (Di Celma *et al.* 2017), a time interval between 18.8 and 18.0 Ma can be provided, corresponding to the late early Burdigalian (late Early Miocene) (see Biostratigraphy section below and Appendix 1).

Derivation of name. Honouring the discoverer of the holotype MUSM 1980, the Peruvian artist Álvaro Suárez Vértiz.

Diagnosis. *Inticetus vertizi* differs from other odontocetes in the following presumed autapomorphies: presence of a high rim around the internal acoustic meatus of the periotic; large fovea epitubaria on the periotic with a correspondingly voluminous accessory ossicle of the tympanic bulla and short anterior bullar facet (also present in physeteroids); shortened tuberculum of the malleus (also present in eurhinodelphinids, physeteroids, and ziphiids); reduced ornament of dental crowns; and relatively high number of large, broad-based accessory denticles (up to four mesial and five distal denticles) in posterior cheek teeth (also present in *Neosqualodon*). Other derived characters relevant to early odontocetes include: bony nares being located far posterior to level of antorbital notch and roughly vertical; nasals being proportionally anteroposteriorly short; the intertemporal constriction being most likely absent; lower tooth count being at least 18 teeth per quadrant. Additional, probably plesiomophic characters include: absence of a pterygoid-maxilla contact on the palate; styliform process of the jugal being markedly robust; sutural contact of the jugal with the zygomatic process of the squamosal being long; presence of a deep notch separating the basioccipital crest from the falcate process of the exoccipital; posterior increase of the height of the mandible being gradual; and incisors being not procumbent.

Description

Ontogeny

No vertebra from any region of the column could be found with a detached epiphysis. With suture lines between centrum and epiphysis occasionally clearly visible in some thoracic, lumbar, and anterior caudal vertebrae (intermediate between states C and D of Galatius & Kinze 2003), we consider this individual as young to fully adult, an interpretation further supported by the robust aspect of all cranial bones and the thick layer of cement covering dental roots.

Total body length estimate

To estimate the total body length (tbl) of MUSM 1980, we used two equations provided by Pyenson & Sponberg (2011) based on the bizygomatic width (bzw, estimated at 36 cm for MUSM 1980): one equation established for stem Odontoceti "log(tbl) = 0.92 * (log(bzw) – 1.72) + 2.68" and the other for stem Platanistoidea "log(tbl) = 0.92 * (log(bzw) – 1.51) + 2.49". The two calculations yielded similar results for tbl, 3.38 and 3.41 m. This is slightly larger than the estimate for *Prosqualodon davidis* calculated by Pyenson & Sponberg (2011), in the upper part of the range for the extant delphinid *Tursiops truncatus* (Wells & Scott 1999). Measurements taken in the field indicate a length of the skeleton (from the apex of the rostrum to the last caudal vertebra) of about 4 m. Significantly higher than the values obtained using the Pyenson & Sponberg (2011) equations, such a value could be due, at least in part, to the slight disarticulation of the skeleton, which probably resulted in a minor shift of the skull compared to the postcranial skeleton (see below).

Skull

The cranium and mandible underwent some degree of deformation. On the one hand, the well-preserved rostrum and mandibles are moderately obliquely compressed, as indicated by the dorsal part of the right premaxilla being slightly below the left premaxilla and the right mandible being markedly lower than the left in the symphyseal region (Figs 3-5). On the other hand, the neurocranium is dorsoventrally flattened, as indicated by the marked dorsoventral crushing of the left orbit, temporal fossa, and mandibular ramus (Figs 4-8). In addition, the dorsal surface of the neurocranium was exposed for some time at the surface of the outcrop. As a consequence, bones of the facial region and supraoccipital shield are heavily worn and partly dislocated (Fig. 3), rendering the interpretation of most sutures and other morphological features (including the assessment of the degree of asymmetry) from these regions dubious; this condition contrasts with the much better preservation state of the basicranium. Most of the teeth are still in situ or only slightly shifted from their original position in alveoli; the distance from the original position is higher in upper teeth from the right side and all the lost/detached teeth originate from the upper jaws. The left mandibular condyle is in connection with the left mandibular fossa of the squamosal and the left lacrimojugal complex is slightly shifted posteroventrally (Fig. 6). The right orbit is lost and the right part of the basicranium is severely damaged.

Cranium

General morphology. The relatively large cranium is characterized by an elongated rostrum, making 64 per cent of the condylobasal length (Table 1). The anterior part of the rostrum is robust and the gradual posterior widening of the latter leads to a broad rostrum base. The upper tooth count is at least 15, as seen on the right side (three incisors, one canine, and at least 11 cheek teeth; see details below); this is at least five teeth more than the basilosaurid condition, corresponding thus to moderate polydonty. The mesorostral groove is widely open at the rostrum base and the bony nares are located far (c. 135 mm) posterior to the level of the antorbital notch. Whereas the dorsoventral extent of the temporal fossa cannot be assessed, the fossa is anteroposteriorly long (length estimated to 140-150 mm on the left side), longer than the partly dislocated corresponding orbit.

Premaxilla. The anterior part of the rostrum is made of the premaxillae alone (Figs 3, 4, 13-15). Each premaxilla bears alveoli for three non-procumbent, ventrolaterally directed incisors. The ventral margin of each premaxilla converges anterodorsomedially, and the maximum transverse width and dorsoventral height of each premaxilla in this region is at the level of I^3, with an oblique dorsomedial to ventrolateral width of more than 44 mm on the right side (Fig. 4). Right and left premaxillae are not fused dorsomedially above the mesorostral groove, but they were probably originally either contacting each other or only leaving a narrow medial gap for the anterior half of the rostrum. In this region, the dorsolateral surface of each premaxilla is pierced by a series of small to medium sized foramina (at least seven on the right side and six on the left side), followed anteriorly by sulci of varying length. The dorsomedialmost sulcus is the longer on each side (more than 80 mm). Visible throughout most of the rostrum, the premaxilla-maxilla suture leaves from the ventrolateral margin of the rostrum between I^3 and the upper canine in a posterodorsomedial direction; the dorsal and lateral exposures of the premaxilla decrease thus until about mid-length of the rostrum. From this level, each premaxilla widens gradually posteriorly. Unfortunately, the dorsal surface of the proximal part of the rostrum is damaged, and sutures are more difficult to follow, especially on the right side. The convex lateral margin of the left premaxilla posterior to the level of the antorbital notch is an indication for the presence of a long and proportionally wide premaxillary sac fossa with a roughly straight medial margin. However, no premaxillary foramen and associated sulci could be detected. Left and right premaxillae are widely spaced anterior to the bony nares. This wide dorsal opening of the mesorostral groove (c. 47 mm anterior to the presphenoid) may have been be slightly exaggerated by the dorsoventral

flattening of that region of the cranium. Based on the preserved parts, each premaxilla is proportionally transversely wide in front of the nasal and it most likely contacted the corresponding frontal at the vertex (Fig. 3).

Maxilla. The upper surface of the maxilla is well preserved only along the anterior half of the rostrum; its dorsal exposure gradually widens posteriorly as shown by the oblique maxilla-premaxilla suture (Fig. 3). In this region, the lateral margin of the maxilla is marked by notches corresponding to the spaces between maxillary alveoli housing crowns of mandibular teeth (shallow embrasure pits). On the left side, the six anteriormost maxillary alveoli (including the canine and five cheek teeth) extend on a length of 210 mm; those alveoli open ventrolaterally. A laterally located embrasure pit for the right C_6 is still visible between C^5 and C^6, whereas the embrasure pit for C_7 extends less dorsolaterally between C^6 and C^7, and more posterior embrasure pits (starting at C_8) are medial to the upper tooth row. In relation to this pattern, the spacing between maxillary alveoli decreases gradually posteriorly, from a distance of 16.4 mm between right C^7 and C^8 to less than 3 mm between C^{10} and C^{11}. If present, more posterior maxillary alveoli are hidden by the mandible.

The antorbital notch is better preserved on the left side, where it is followed posteriorly by a wide sulcus (Fig. 3). The lateralmost part of the maxilla in the supraorbital region is probably missing on the two sides, but less incomplete on the left. The left maxilla reaches posteriorly the level of the occipital condyles. However, this projection posterolateral to the supraoccipital shield is most likely exaggerated by the dorsoventral crushing of the neurocranium. The presence of a left posterior dorsal infraorbital foramen is suspected several centimeters posterolateral to the left premaxilla.

On the palate, the joined maxillae form a broad (transversely wider than the anteriormost width of the palatines), roughly flat surface anterior to the palatines, well demarcated from the more posterodorsolateral regions by posteriorly converging palatal ridges (Fig. 5). Each maxilla is pierced by at least one palatine foramen a short distance anterior to the anterolateral corner of the palatine.

Presphenoid. At the posterior end of the mesorostral groove, the ossified portion of the presphenoid (= mesethmoid in many previous works; see Ichishima 2016) is short, ending c. 90 mm posterior to the level of the antorbital notch, and roughly as wide transversely as the maximum dorsal opening of the mesorostral groove. The preserved part of the nasal septum is surprisingly wide, broader than the adjoining narrow bony naris (Fig. 3). Such a wide

separation of the bony nares may also be linked to the dorsoventral crushing and abrasion of this region, with the artificial exposure of a more ventral region of the septum.

Vomer. The vomer could not be detected in the mesorostral groove. Ventrally, it appears between the maxillae from a level 60 mm anterior to the palatine, widening moderately anteriorly (Fig. 5). Posterior to the choanae, an undulating transverse suture is interpreted as the vomer-basisphenoid suture.

Nasal. Two small (less than 3.5 mm wide), somewhat nodular bones posterior to the nasal septum and at a longitudinal level just posterior to the tip of the zygomatic process of the squamosal most likely correspond to the nasals (Fig. 3). Each nasal sends a robust anterolateral projection, seemingly more pointed on the right side. Although the posterior portion of the nasal is dorsoventrally thin, this may be a consequence of the superficial abrasion of the dorsal surface.

Frontal. The vertex of the cranium being too damaged, no specific features of the dorsal exposure of the frontals can be detected, except that they may have been anteroposteriorly longer than the nasals.

Preserved on both sides, the massive and roughly vertical postorbital process of the frontal has a dorsoventral height greater than 37 mm (Figs 4, 6). Due to the shift of the lacrimojugal complex and the partial preservation of the maxilla and frontal in the left antorbital region, the anteroposterior length of the orbit cannot be estimated. There is nevertheless no indication for a reduced size of the latter.

Palatine. The anterior portion of well-defined palatine-maxilla suture zigzags with a mean lateral direction until the palatal ridge, where it turns abruptly posterolaterally (Fig. 5). The anterior end of the palatine is slightly anterior to the antorbital notch and 60 mm anterior to the tip of the pterygoid sinus fossa.

Pterygoid. Only a small part of the lateral lamina of the pterygoid may be visible on the right side, forming the lateral wall of the pterygoid sinus fossa (Fig. 5). Considering the great distance between the fragments of pterygoid around the fossa and the palatine-maxilla suture, a contact between pterygoid and maxilla on the palate can be ruled out in MUSM 1980, which differs on that point from many platanistoids (e.g., *Platanista*, *Pomatodelphis*, *Squalodon*, and

Zarhachis; see Muizon 1987, 1994). Anterior to the choana, the pterygoid sinus fossa is wide and relatively long, with a maximum ventromedial to dorsolateral width of 56 mm and an anterior tip 50 mm before the choana, just posterior to the level of the antorbital process. The thin plates of pterygoids anterolaterally margining the choanae are partly dislocated and slightly shifted from their original position. Although partly crushed, the medial lamina of each pterygoid is preserved until its posterior contact with the basioccipital crest.

Lacrimal/jugal. In the left orbital region, the lacrimojugal complex is shifted posteroventrally from its original position (Figs 4, 6). Jugal and lacrimal are probably fused, with no suture apparent, and make a massive bone anteriorly limiting the orbit. The base of the styliform process is wide and thick, whereas the process itself becomes thinner posteriorly, yet retaining a great width (24 mm wide just anterior to the zygomatic process of the squamosal, for a thickness of 3 mm for the lateralmost part of the process). The contact surface of the jugal with the ventral margin of the zygomatic process is long, c. 40 mm.

Supraoccipital. The outline of the fragmented and abraded dorsomedial part of the supraoccipital shield cannot be reconstructed. Best seen in posterior view (Fig. 8), only the ventrolateral region is partly preserved, with both temporal crests converging anterodorsomedially, corresponding to widely posteriorly open temporal fossae.

Squamosal. In lateral view, the zygomatic process is anteriorly long; the supramastoid crest rising slightly anterodorsally; and a bulge located at mid-length of the ventral margin corresponds to the end of the jugal-squamosal suture (Figs 4, 6). The maximum dorsoventral height of the process at the level of that bulge is 41 mm. Best seen in anterior view, a deep longitudinal notch marking the anterior part of the ventral margin originally housed the posterior part of the styliform process of the jugal. The postglenoid process is ventrally long, with a vertical height of the squamosal at that level reaching 98 mm. Distinctly curved anteroventrally, the apex of the process makes a robust, yet anteroposteriorly flattened blade that ends ventrally before the level of the ventral margin of the exoccipital (Figs 6, 7). The medial surface of the postglenoid process is slightly concave, forming a shallow depression possibly corresponding to an extension of the tympanosquamosal recess. The posttympanic process is not much extended anteroposteriorly and is ventrally shorter than the exoccipital. At least one sternocephalicus fossa (see Cotton *et al.* 2008 for terminology) excavates the posterolateral surface of the bone. The external acoustic meatus is relatively wide and

transversely long. Better preserved on the left side, the falciform process is a large plate (maximum length = 45 mm) with deeply indented margins.

Basisphenoid. A posteriorly convex suture halfway between the vomer and the posterior end of the basioccipital crest in the basioccipital basin is tentatively interpreted as the basisphenoid-basioccipital suture (Figs 5, 7).

Basioccipital. Low anteriorly, the relatively thin ventral margin of the basioccipital crest rises abruptly posteroventrolaterally. The ventralmost part of the crest is anteroposteriorly short, smoothly curving posterolaterally and then posteromedially. The crest is separated from the falcate process of the exoccipital by a deep oblique notch (Figs 7, 8). Left and right crests diverge markedly, limiting a widely posteroventrally open basioccipital basin.

Exoccipital. Posteromedial to the posttympanic process of the squamosal, the exoccipital is bulky. In ventral view, the cylinder-shaped paroccipital process of the exoccipital is robust, with transverse and anteroposterior diameters of the left process of 61.0 and 41.5 mm, respectively (Fig. 7). The ventral surface of the process bears a similarly large articulation facet for the stylohyal. The anterior surface of the process lacks any paroccipital concavity for the posterior sinus. As in basilosaurids, the falcate process of the exoccipital is distinct from the basioccipital crest; it is shorter ventrally than the latter. A vestigial falcate process of the exoccipital is described in a few stem physeteroids, much more reduced than in MUSM 1980 (Lambert *et al.* 2016). Best preserved on the right side, the jugular notch is wide and somewhat proportionally deeper, with an oval outline in posterior view. The occipital condyles are robust, with a short condylar neck.

Periotic. Only the right periotic of MUSM 1980 could be observed (Fig. 9; Table 1), as the left is still in situ, dorsal to the corresponding tympanic bulla attached to the basicranium. The right periotic is nearly complete; only some small fragments are missing at the apex of the posterior process and along the ventral surface of the anterior process just anterior to the fovea epitubaria. The facial sulcus could not be completely prepared, due to the presence of the stapes lying in the sulcus, posterolateral to the fenestra vestibuli (= fenestra ovalis).

The ventral surface of the anterior process is excavated by a vast and deep fovea epitubaria, housing the large, detached accessory ossicle of the tympanic bulla (see below). The fovea epitubaria is defined (1) laterally by an acute, thin crest, (2) medially by a slightly

more robust crest, (3) posteriorly by the high anterior margin of the mallear fossa, and (4) anteriorly by a prominent tuberosity. This tuberosity is margined laterally by a shallow groove just medial to the acute crest mentioned above. Most likely housing part of the outer lip of the tympanic, this groove turns anteromedially around the tuberosity and is followed by a small, roughly circular fossa (transverse diameter 3.2 mm) interpreted as a very small anterior bullar facet, as observed in many physeteroids. The roughly flat ventrolateral surface of the anterior process is exposed in ventral view, marked by a series of thin grooves (at least nine); posterior grooves are transversely oriented whereas more anterior grooves are anterolaterally and then anteriorly directed. No conspicuous parabullary sulcus (*sensu* Tanaka & Fordyce 2014) could be identified in this region. This ventrolateral surface is separated from the lateral tuberosity by a wider, shallow groove, probably corresponding to the anterolateral sulcus described in *Simocetus* (Fordyce 2002; anteroexternal sulcus *sensu* Tanaka & Fordyce 2014). However, it should be noted that the posterolateral part of the parabullary sulcus has been illustrated as nearly continuous with the anteroexternal sulcus in some odontocetes (see Tanaka & Fordyce 2016), making the distinction between these two features more difficult to define.

In medial view, the anteroventral apex of the anterior process is markedly projected ventrally as compared to the proximal part of the process. The medial surface of the process is weakly concave in the area dorsal to the prominent tuberosity.

In lateral view, the apex of the anterior process is clearly inflated as compared to its base, which is markedly constricted on its dorsolateral surface just anterior to the lateral tuberosity (level of anteroexternal sulcus). This feature is partly related to the presence of a wide, obliquely oriented depression on the dorsal surface of the bone, separating the anterior process from the pars cochlearis. The anterodorsal region of the anterior process is prominent, but no anterodorsal angle is observed (area smoothly rounded in lateral view).

As a result of its complex morphology, the outline of the transverse section of the anterior process changes markedly along its longitudinal axis: this section is distinctly mediolaterally wider than dorsoventrally high at its base (17.4 vs. 11.0 mm), roughly as mediolaterally wide as dorsoventrally high at mid-length (14.0 vs. 13.0 mm), and much dorsoventrally high than mediolaterally wide in its anterior section. A small tubercle (transverse diameter 3.3 mm) is located medioventrally at the contact between anterior process and pars cochlearis, anteroventral to the cerebral opening for the facial canal (Fig. 9B). It is followed anterodorsally by a short (5.0 mm) crest.

The large, subrectangular ventral surface of the lateral tuberosity is flat to slightly concave. Whereas the lateral surface of the tuberosity is only separated from the lateral

margin of the anterior process by a smooth concavity in ventral view, the posteroventral margin of the tuberosity has an angular border with the moderately deep hiatus epitympanicus. The vast, oval, and posteromedioventrally facing mallear fossa has a maximum diameter of c. 7 mm. The well-defined fossa incudis has a maximum diameter of c. 2 mm. It is separated from the mallear fossa by another small (maximum diameter of c. 2 mm), shallower, and anteroventrolaterally facing depression. This small fossa matches well the shape and position of the submallear fossa described between the mallear fossa, the fossa incudis, and the ventral opening of the facial canal (= secondary facial foramen) in the New Zealand platanistoids *Awamokoa tokarahi* and *Waipatia maerewhenua* by Tanaka & Fordyce (2017). Posterior to the fossa incudis is a prominent small tubercle corresponding to the anterior end of the posterior bullar facet.

The anterior margin of the ventral opening of the facial canal is slightly anterior to the anterior margin of the fenestra vestibuli. The outline of the fenestra vestibuli is oval. The stapedius muscle fossa is dorsally deep, but it does not excavate the medial surface of the posterior process. Between the hiatus epitympanicus and the anterolateral surface of the posterior process, a thick, oblique ridge extends in an anteromedial direction. Marked by a series of thin grooves, this ridge probably corresponds to a low articular rim (see Muizon 1987, 1994). Although a small break surface limits the posterolateral extent of this ridge, a hook-like articular process was most likely not present.

Whereas the long axis of the posterior process is directed posteroventrolaterally, the surface of the posterior bullar facet is roughly flat, lacking any longitudinal concavity (a feature observed for example in ziphiids) and any transverse convexity (a feature observed in physeteroids). The surface of the proximal region is marked by four to five shallow grooves, barely reaching half the length of the process. In medial view, the dorsal margin of the posterior process curves smoothly posteroventrally. The distal portion of this margin is keeled for at least 14 mm, displaying a triangular transverse section.

In ventral view, the pars cochlearis is proportionally wide and only moderately medially elevated, not taking account of the high rim defining part of the internal acoustic meatus (IAM); its outline is generally rounded, except for a barely marked posteromedial angle. Ventral to the ventral wall of the IAM, the dorsoventrally wide (9.0 mm) medial surface of the pars cochlearis is nearly flat. The fenestra cochleae (= fenestra rotunda) is renifom to crescent shaped, with a first groove leaving dorsally from the lateralmost tip and a second groove leaving dorsomedially from the medialmost tip. Between the fenestra cochleae and the stapedius muscle fossa, a thick bar of bone extends anteriorly along the ventromedial

edge of the fenestra vestibuli and floors the medial edge of the stapedius muscle fossa. This crest represents the crista interfenestralis as identified by O'Leary (2010), which is generally well developed in cetaceans. As mentioned by Mead & Fordyce (2009, p. 115) "in *Tursiops* … the crista interfenestralis merges back into the indistinct caudal tympanic process". The structure labelled as "cochlear crest" by Fordyce (2002, fig. 15) and "caudal tympanic process" by Tanaka & Fordyce (2015b, fig. 13) is the posterior extension of the crista interfenestralis and corresponds to the lateral caudal tympanic process as defined by MacPhee (1981, p.17-18). As described by O'Leary (2010), the caudal tympanic process of cetaceans is a mediolaterally broad and low thickening on the posterodorsal edge of the fenestra cochleae and represents the medial caudal tympanic process (MacPhee, 1981, p. 17 and fig. 2; Muizon *et al.* 2015, figs. 37-39, 50). The medial caudal tympanic process is generally low or absent in odontocetes. In *Inticetus*, however, the posterodorsolateral edge of the fenestra cochleae is bordered by a thick ridge, which extends posterodorsally and which is separated from the crista interfenestralis. We interpret this ridge as a medial caudal tympanic process. The lateral caudal tympanic process (*sensu* MacPhee 1981, fig. 2), which, in cetaceans, merges with the posterior extension of the crista interfenestralis, is poorly developed in *Inticetus*: the crista interfenestralis lacks a distinct posteroventral angle and only bears a tiny spine directed posteroventrolaterally above the stapedius muscle fossa.

The small and transversely elongated aperture for the cochlear canaliculus (= cochlear aqueduct) (2.5 x 1.2 mm) opens mediodorsally, but is more ventral than the ventromedial margin of the IAM. Its dorsal margin is part of a prominent area between this aperture and the aperture for the vestibular aqueduct (= endolymphatic duct). Much larger (4.6 x 2.7 mm), the latter is closer to the IAM. In the IAM, the large and anteriorly pointed opening for the facial canal (3.5 mm of diameter) is more anterior than the tractus spiralis foraminosus, giving the IAM an anterolaterally elongated outline. The thick transverse crest separating the opening for the facial canal from the tractus spiralis foraminosus is moderately elevated, distinctly lower than the surrounding dorsal surface of the periotic.

On the anterior flank of the transverse crest, posterior to the dorsal aperture of the facial canal, is a small, circular depressed area, which probably represents the anterior meatal pit, variably present in *Tursiops* (Mead & Fordyce 2009, p.112 and fig. 25). On the posterior edge of the transverse crest is a large foramen singulare, which was apparently partly open posteriorly. The margins of the IAM form a high rim, thick at its base, around the tractus spiralis foraminosus; such a tube-like mediodorsal extension of the tractus differs from the cochlear spine observed in the ziphiids *Berardius* and *Ninoziphius*, both for its shape and

position. A similar condition is observed in *Remingtonocetus* and several protocetids (e.g., *Carolinacetus* and *Georgiacetus*; Geisler *et al.* 2005), as well as in the tooth-bearing mysticete *Mammalodon* (Fitzgerald 2010, fig. 23b); this character may thus be primitive among neocetes, although it is not present in basilosaurids (see Kellogg 1936; Luo & Gingerich 1999) and other archaic odontocetes for which this region is observable (Park *et al.* 2016; pers. obs.).

The dorsal process forms a low dome with a tip 10 mm distant from the aperture for the vestibular aqueduct in a posterolateral direction. A small foramen along the lateral surface of the dome may correspond to the posteroexternal foramen identified medial to the incipient articular rim in *Waipatia* (Fordyce 1994). Medial to the top of the dorsal process is another small opening, possibly a foramen too.

Tympanic bulla. The left tympanic bulla was kept in situ in the basicranium, where it is probably somewhat anterodorsally shifted from its original position (Figs 5, 7); a few measurements were taken on this side (Table 1), but most observations come from the detached right tympanic (Fig. 10). The latter is nearly complete: only fragments of the outer lip, dorsomedial fragments of the sigmoid process, the anterior part of the posterior process, and a tiny part of the incipient anterior spine are missing. The accessory ossicle is detached from the outer lip. In addition, the region of the sigmoid process is slightly crushed over the conical process and the anterior part of the outer lip is shifted slightly medially and separated from the posterior part of the lip by a vertical break.

In ventral view, inner and outer posterior prominences have the same posterior extent; the inner prominence is more pointed and somewhat narrower. A slight and rather irregular ventral keel marks the ventral surface of the latter, extending anteriorly on c. two-fifths of the length of the bone. The median furrow is broad and proportionally shallow for its whole extent, being barely visible 8 mm from the anterior tip of the bone. Based on the observation of the dorsoventrally thin anterior section, the anterior spine was most likely incipient, forming a narrow and thin plate associated to a distinct anterolateral concavity.

In medial view, the ventral margin of the involucrum is convex and somewhat irregular, with a slight notch at the posterior fourth of its length. The dorsal margin rises abruptly from the incipient anterior spine, reaching a shelf that rises only slightly posterodorsally. The medial and dorsal surfaces of the involucrum are crossed by a series of transverse grooves. In dorsal view, one of these grooves corresponds to a clear step at the

anterior third of the length of the bone, but this abrupt transverse widening is not visible in medial view.

In lateral view, although the outer lip is somewhat damaged its original dorsal extent was not much greater than the preserved condition. The lateral furrow is partly obscured by hardened sediment. The sigmoid process is located high along the outer lip and its posteroventral margin makes a smooth open curve, lacking any posteroventral corner. Partly hidden by the sigmoid process, the conical process is massive and transversely much wider than the preserved part of the sigmoid process. In posterior view, the elliptical foramen is widely open and vertically elongated.

On the posterior process, the surface of the facet for the posterior process of the periotic faces posteromediodorsally. Its medial region is marked by a wide and proportionally shallow, posterolaterally directed groove, perfectly matching a low ridge in the medial part of the posterior bullar facet of the periotic. On the lateral part of the posterior process, either some small fragments of the basicranium are attached (possibly elements of the posterior meatal crest), or the surface of contact with the basicranium is damaged.

The detached accessory ossicle is large, dorsoventrally flattened, and slightly elongated (maximum length of 13.0 mm, including a fragment of outer lip attached, maximum transverse width of 11.5 mm, and maximum dorsoventral thickness of 6.6 mm) (Fig. 9). Its outline is subcircular in ventral view (without the fragment of outer lip) and oval in medial view. Positioned on the periotic, it projects anteromedioventrally.

Malleus. Apart from fragments of the anterior and posterior facets for the incus and the distal part of the anterior process, the right malleus of MUSM 1980 is finely preserved (Fig. 11). Total height in posteroventromedial view is 8.0 mm, including 5.1 mm for the articular head (bearing the facets for the incus). The tuberculum is thus markedly reduced compared to other odontocetes except eurhinodelphinids, physeteroids, and ziphiids (Muizon 1985; Lambert 2005; Bianucci *et al.* 2010). Maximum width of the bone across the articular head is 6.8 mm, including 4.9 mm for the joined anterior and posterior facets. The posterior facet is slightly higher and transversely narrower than the anterior facet. On the same side as the anterior facet, the tuberculum bears the well-defined muscular process (for insertion of tendon for muscle tensor tympani); the latter is lower than the manubrium (the vertical being taken along the line separating anterior and posterior facets), a condition reminiscent of platanistoids (e.g., *Notocetus*, *Pomatodelphis*, and *Squalodelphis*; Muizon 1985, 1987) and differing from

delphinidans, physeteroids, and ziphiids. At the top of the tuberculum, the manubrium makes a massive cone. The base of the broken anterior process is high relative to the posterior facet.

Stapes. The small bone preserved in the facial sulcus of the right periotic posterolateral to the fenestra vestibuli is most likely the right stapes (Fig. 9). Apart from the oval umbo visible in anteroventral view, no further morphological features can be observed.

Mandibles

Although the symphyseal portion of the two mandibles is finely preserved, due to dorsoventral compression both rami are more fragmented and, for the better-preserved left ramus, partly obscured by the lacrimojugal complex and squamosal. As a result, the dorsal outline of the ramus could not be reconstructed.

The long symphyseal portion of the mandible makes 44 per cent of the total length, ending at a level between C_6 and C_7 (Fig. 5; Table 1). Right and left mandibles are not ankylosed and the flat ventral part of the symphyseal surface is visible along the ventrally shifted right mandible. In lateral view the ventral margin of the mandible makes a straight line for most of its length, rising abruptly anterodorsally from the level of I_2. The ventromedial margin of each mandible is marked by a longitudinal crest for 30 mm distally. Numerous mental foramina are observed on each side, followed anteriorly by sulci; a total of about 13-14 foramina are counted on the right side, with anterior foramina concentrated along the ventral margin of the bone and more posterior foramina rising posterodorsally. Mental foramina extend posteriorly beyond the level of C^{11}, as seen on the right side.

Matching tooth counts on the upper jaw, alveoli for three lower incisors and one canine are identified, with I_1 being located anterior to I^1. Posterior to the lower canine, alveoli for right cheek teeth C_1-C_9 are visible in lateral view (Fig. 4), whereas alveoli for right C_7-C_{14} are visible in medial view. The total lower tooth count is thus at least 18 teeth. The alveolus for I1 opens dorsally and slightly anteriorly, but it does not correspond to a procumbent tooth. Alveoli for more other teeth open dorsally and slightly laterally. Whereas anterior lower teeth are widely spaced, alternating with upper teeth, spacing decreases from the level of C_7; from C_8 to C_{14}, interalveolar space is highly reduced, with crowns of succeeding teeth nearly contacting each other. Although the left angular process is fragmented and tilted under the mandibular condyle, its extent indicates that the condyle was originally at some distance from the ventral margin of the mandible, differing on this point from physeteroids. The mandibular condyle is robust; its marked lateral projection (27 mm) may have been exaggerated due to

partial dislocation. The outline of the left coronoid process is visible in medial view. This process rises only gradually and moderately posterodorsally. The anterior and anterodorsal margin of the enlarged mandibular foramen is preserved on both sides.

Teeth

As detailed above, the upper dental formula is three incisors, one canine, and more than 11 cheek teeth, totalling more than 15 teeth, and the lower dental formula is three incisors, one canine, and at least 14 cheek teeth, totalling at least 18 teeth.

Incisors. The right I^1 is detached (Fig. 12A-F) and all other incisors are in situ in the premaxillae and mandibles (Figs 13-15). All incisors are moderately curved, with the root projecting distolingually; for in situ teeth the long axis of the crown is approximately vertical. The root is considerably longer than the crown (Table 2). The height of the conical crown increases slightly posteriorly along the incisor row and the mesiodistal diameter at crown base is slightly greater in upper incisors as compared to lower incisors. When available, the labiolingual diameter at crown base is lower than the mesiodistal diameter. The crown of all the incisors bears a clear mesial carina; the distal carina is less distinct, constituted by a slightly higher longitudinal ridge as compared to the rest of the crown. None of the carinae is serrated. All surfaces of the nearly smooth enameled crown are ornamented by slightly undulating, low longitudinal ridges. In I^1, the ornamentation is slightly more conspicuous along the lingual and distolingual surfaces and towards crown base, most likely due to differential abrasion wear.

Along a break section close to the root-crown boundary of right I^2, a thick layer of cement (c. 0.5 mm) is measured. Additionally, the root of right and left I^1 is marked by a distinct mesial bulge close to the root-crown boundary.

Canines. The right upper canine is detached, with the lingual surface damaged (Fig. 12G-L) and all other canines are in situ in the maxillae and mandibles (Figs 13-15). The root of the right upper canine is proportionally slightly shorter, stockier than the root of I^1. No significant size differences are noted for canine crowns as compared to incisors, and the labiolingual diameter at crown base is similarly lesser than the mesiodistal diameter (Table 2). As in incisors, the mesial carina is somewhat more conspicuous than the distal carina.

Cheek teeth. Anteriormost cheek teeth do not differ significantly from canines. From C^1 and C_1, the maximum mesiodistal diameter in the crown base region increases gradually posteriorly, with the maximum size attained in C^{10} (C^{11} incomplete) and C_9 (decrease of size in C_{10} and next lower teeth partly obscured). In a similar way, the height of the crown increases until C^5 (more posterior upper cheek teeth obscured) and, in a less regular way along the lower row, until C_{10} (C_{11} obscured) (Table 2). For the better observable lower tooth rows, the mesiodistal diameter at crown base becomes greater than crown height in the interval between C_5 and C_9, with a ratio between the two measurements of 0.94 in C_5, 1.72 in C_9, and 1.60 in C_{10}.

Along the upper tooth row, a tiny accessory denticle may have occurred at the base of the distal carina of C^4 (area slightly damaged) (Fig. 14). On the left C^5 (better-preserved than the right; Fig. 15), a slight bulge at the base of the mesial carina bears two tiny denticles, whereas the widened base of the distal carina bears about six tiny denticles. The base of the mesial carina of C^6 bears at least one small denticle, whereas at least three distinctly larger accessory denticles, decreasing in size towards crown base, are observed along the distal carina (Table 2). As in the next cheek teeth of the upper tooth row, these large and labiolingually robust accessory denticles display a mesiodistally broad base and these considerably increase the labial/lingual surface of the proportionally wide crown. The condition in C^7 is nearly identical to C^6, with two-three tiny denticles along the mesial carina and three larger accessory denticles along the distal carina (Fig. 16); a tiny denticle is observed at the base of distal carina of the most apical of these distal accessory denticles. The mesial carina of C^8 bears three large accessory denticles, with one tiny denticle at the base of the medial carina of the two basalmost accessory denticles, and the distal carina bears at least three large accessory denticles. In C^9, three large accessory denticles are present along the mesial carina, and at least two along the distal carina (base damaged). In C^{10}, three accessory denticles are visible along the mesial carina: the basalmost is smaller and an additional mesial denticle may be present before the apical denticle. At least two accessory denticles are present along the distal carina (apex of the tooth obscured by the mandible). C^{11} is nearly completely hidden by the mandible. Only the labial surface of the crown is available for these upper cheek teeth; no cingulum or other labial ornamentations are present. Only the lower part of the roots of upper cheek teeth is visible. C^3 is single-rooted, and although a partial separation of mesial and distal roots by a longitudinal groove appears in C^4, we could not identify the level at which two apically separated roots appear.

Along the lower tooth row, a distinct widening is observed at the base of the crown in C_2, C_3, and C_4, with mesioventral and distoventral bulges of the enamel becoming larger posteriorly (Figs 14, 15). In C_5, the base of the mesial carina may bear a tiny denticle; a better-defined, larger denticle is present at the base of the distal carina, possibly bearing several tiny denticles as suggested by the observation of several longitudinal ridges in this area. Several tiny denticles are most likely present at the base of the mesial carina of C_6, and one larger accessory denticle bears about four tiny denticles at the base of the distal carina. The crown of the right C_7 is partly hidden in labial view, but shows at least two large accessory denticles along the distal carina. Better seen in lingual view (Fig. 17), C_8 bears three large accessory denticles along the mesial carina and four along the distal carina, with an additional smaller denticle at the base. As for posterior upper cheek teeth, the broad-based large denticles increase the labial/lingual surface of the crown; a line passing through the apices of succeding denticles gives a broadly open ogival outline. The mesial carina of C_9 bears an additional smaller denticle at the base of the mesial carina, and five denticles along the distal carina. Four denticles are present along the mesial carina of C_{10}, and five along the distal carina. Partly obscured by C_{10}, the mesial carina of C_{11} bears at least three denticles, whereas five denticles are present along the distal carina. In both C_{12} and C_{13}, the distal carina bears at least three denticles.

The labial surface of C_1-C_7 and the lingual surface of C_8-C_{13} lack any indication of a cingulum; only fine, shallow longitudinal ridges are observed.

As for upper cheek teeth, roots are only partly visible. A slight depression between mesial and distal roots appears in C_4; the groove separating the two roots is deeper in C_5, with a mesiodistally broader exposure of the roots; lower cheek teeth are probably double-rooted from C_6 (more conspicuous in C_7).

None of the upper and lower teeth displays unambiguous wear facets; when preserved, the apex of the crown and accessory denticles is intact; only the fine longitudinal grooves ornamenting the labial and lingual surfaces of teeth are occasionally slightly attenuated, most likely due to abrasion.

Vertebrae

The preservation state of the vertebrae is in general not good; due to a long period of exposure at the surface, many processes and even parts of centra were worn away. Furthermore, part of the vertebrae display clues for post-burial deformation, which leads to some degree of uncertainty for the measurements. The vertebral series is most likely not complete. The

posterior half portion of the vertebral column was still nearly perfectly articulated in the field. Consequently, for this part it was easy to reconstruct the original position of the vertebrae. Instead, the anterior half portion was partly disarticulated prior to collection and the original sequence was tentatively reconstructed after measuring and comparing the vertebrae. Therefore, the sequence as presented here and in Table 3 for thoracics (ThI, ThII, ...), lumbars (LuI, LuII, ...), and caudals (CaI, CaII, ...) should be considered as tentative (and therefore indicated with Roman numbers instead of Arabic numbers).

Cervicals. Only the right side of the atlas is preserved, including the anterior and posterior articular facets, the transverse processes, and part of the neural arch (Fig. 18). The maximum anteroposterior length as preserved is 59 mm; the maximum height of the posterior articular facet is 55 mm. The dorsal transverse process is not as well preserved as the ventral process; both processes were most likely not much elongated with a roughly similar lateral extent. Atlas and axis were not ankylosed.

The right side and the ventral portion of the free axis are preserved in a single block together with cervicals C3-C5 (Fig. 19). The maximum anteroposterior length of the axis as preserved is 41 mm; the maximum width is estimated at 142 mm. The transverse process forms a dorsoventrally high, subrectangular and posterolaterally projected plate, pierced by a small vertebrarterial canal (maximum diameter = 6.0 mm). The partly preserved odontoid process is robust.

The somewhat more pointed transverse process of C3 is slightly longer than the transverse process of the axis. Both the dorsal and ventral transverse processes of C4 are incomplete; it cannot be ascertained if the large vertebrarterial canal (maximum diameter = at least 19 mm) was originally laterally closed in the latter. The ventral transverse process of C5 curves laterodorsally and most likely originally joined the dorsal process. C6 and C7 are preserved together. The dorsoventrally thin, blade-like ventral transverse process of C6 is long (58 mm along its anterior surface) and directed ventrolateroposteriorly; its apex is moderately thickened. The centrum of C6 and C7 is transversely wider than dorsoventrally high. C7 probably lacks a genuine lower transverse process, only retaining a proportionally short prominence; its dorsal transverse process is a thin, incompletely preserved plate.

Thoracics. Eleven vertebrae are identified as thoracics. The centrum length and height gradually increase posteriorly, with the transverse process becoming lower along the centrum in the posteriormost thoracics (Table 3). With proportions of the epiphyses close to the last

cervicals, ThI is probably the first thoracic, bearing a transverse process projected far posterolaterodorsally (Fig. 20). The neural arch is only well preserved in ThIV, with an anteroposteriorly long neural spine, probably somewhat posteriorly projected. The transverse process of ThIV is higher than the floor of the neural canal and extends far anteriorly, bearing a large fovea for the articulation of the rib. ThX and ThXI are most likely close to the thoracic-lumbar transition, with ThXI only tentatively identified as a thoracic.

Lumbars. Nine lumbars are identified. When available, the centrum length is generally longer than in thoracics (Table 3). Most lumbars are too fragmentary to allow an informative description; only the ventral portion of the centrum is partly preserved in several of them, sometimes with the broad base of the transverse process (Fig. 21). The ventral surface of the centrum is marked by a medial keel in several lumbars (e.g., LuVII and LuVIII).

Caudals. Seventeen caudals are identified (CaI-CaXVII). The facets for the chevron (hemal arch) are barely marked in CaI, which is probably close to the lumbar-caudal transition. The centrum length decreases gradually posteriorly, with a more abrupt reduction from CaXI (Table 3; Fig. 22). Centrum height is greater than length at least in the CaVIII-CaX section; those caudals may correspond to the tail stock, supporting the laterally compressed peduncle region (Buchholtz & Schur 2004). The length of the transverse process is strongly reduced from CaVII; from the same level, the base of the transverse process is pierced by a vertical vertebrarterial canal. The transverse process is roughly absent in CaIX, only making a low and thick crest, also pierced by a vertical canal. A second, oblique foramen leaves from the ventral side of this crest, reaching the ventromedial surface of the centrum, a condition also observed in CaX. The much shorter centrum of CaXI remains dorsoventrally higher than transversely wide.

The five posteriormost caudals (CaXIII-CaXVII) are markedly wider than long or high, corresponding to the fluke region. The lateral surface of these last caudals is incised by a deep longitudinal notch, separating dorsal and lateral swollen regions. On the ventral surface, a depressed medial region is separated by two longitudinal crests; the latter are medial to the vertical vertebrarterial canals. CaXVI and CaXVII were found in tight connection and could not be separated.

Changes in proportions of vertebral centra along the vertebral column. Plotting the dimensions of the vertebral centrum of the best-preserved vertebrae in charts allows

visualizing changes in the proportions of the centra along the vertebral column (see Buchholtz 2001). Although many vertebrae are missing or too incomplete to be measured (resulting in artificially steeper slopes for all the curves), when combining central length, width and height in a single chart (Fig. 23) the result for *Inticetus vertizi* contrasts markedly with the basilosaurid *Cynthiacetus peruvianus*, the latter showing a more gradual, parallel increase for all the dimensions of the centra towards the posterior lumbars and anterior caudals (Martínez-Cáceres *et al.* 2017). Among extant cetaceans, the pattern in *I. vertizi* is more similar to the beluga *Delphinapterus leucas* (see Buchholtz 2001, fig. 5c), characterized by proportionally long posterior thoracics and lumbars. Similarities are even stronger with the large Middle Miocene delphinidan *Hadrodelphis calvertense* (see Buccholtz 2001, fig. 7e). The latter displays a similar increase of the width of cervicals (slightly more posterior in MUSM 1980) and a high peak for the length of posterior lumbars. The available dimensions of the centra match thus well the anatomical pattern 2 as defined by Buchholtz (2001), suggesting a greater flexibility in the anterior torso for *I. vertizi*, more similar to extant Inioidea, Lipotidae, Monodontidae, and Ziphiidae. Finally, similarities with the tooth-bearing mysticete *Aetiocetus cotylalveus* (Buchholtz 2001, fig. 7c) suggest that the condition of *I. vertizi* could be relatively close to the ancestral neocete condition.

Sternum. Two elements of the sternum are preserved, the manubrium and the second sternebra (Fig. 24). The considerably dorsoventrally flattened manubrium (as compared to basilosaurids, see Uhen 2004; Martínez-Cáceres *et al.* 2017) is 163 mm long (maximum anteroposterior length), for a sagittal length of 110 mm and an estimated maximum width of 132 mm. A groove separating the right and left parts is visible on the dorsal and ventral surfaces. The two posterior articular surfaces (for intersternebral cartilage) are slightly dorsoventrally thickened (12-13 mm), compared to the generally thin aspect of all other edges, and separated by a 21 mm deep V-shaped notch. A posteromedial bulge is also observed on the ventral surface, thicker on the left side. The anterolateral region is also slightly thickened.

The Y-shaped second sternebra is smaller, with a maximum anteroposterior length of 91 mm, a sagittal length of 80 mm, and an estimated maximum width of 84 mm, and even more slender than the manubrium. The anterior margin is smoothly concave and the anterolateral region is barely thickened. The posterior surface of articulation is regularly convex and slightly dorsoventrally thickened. Apart from an opening in the centre of the bone, no trace of a sagittal suture is visible.

Ribs. Many rib fragments are preserved, but most are poorly informative. The proximal part of a left anterior rib is well preserved, being widened and flat. Other fragments, either with the articular region or with a slightly more complete body, are illustrated in Figure 25.

Comparison

Inticetus vertizi differs from most other odontocete lineages in a series of skull characters; the most striking differences concern the ear bones and teeth (ornamentation and number and shape of accessory denticles in cheek teeth, see below). Among the ear bone differences, the shortened tuberculum of the malleus is only shared with eurhinodelphinids, physeteroids, and ziphiids (Muizon 1985; Bianucci *et al.* 2010), and the large fovea epitubaria with a correspondingly voluminous accessory ossicle and short anterior bullar facet is seen to a roughly similar extent in physeteroids (e.g., Bianucci & Landini 2006; Lambert *et al.* 2016). However, *Inticetus* differs from all these clades in being heterodont. It further lacks the main cranial synapomorphies of eurhinodelphinids (extreme elongation of the edentulous premaxillary part of the rostrum; e.g., Abel 1901; Lambert 2005), physeteroids (vast supracranial basin and high asymmetry of the bony nares and surrounding bones; e.g., Muizon 1991; Heyning 1997; Lambert *et al.* 2016), and ziphiids (high vertex with transverse premaxillary crests and pterygoid sinus fossa extending anteriorly beyond the level of the antorbital notch and ventrally beyond the ventralmost level of the basicranium; e.g., Lambert *et al.* 2013; Bianucci *et al.* 2016b).

Compared to other heterodont odontocetes, the teeth of *Inticetus* differ from many taxa (e.g., *Agorophius*, *Patriocetus*, *Simocetus*, *Squalodon*, and *Waipatia*) in the reduced ornamentation of the crown (no cingulum and low longitudinal ridges), the relatively high number of large, broad-based accessory denticles (up to four mesial and five distal denticles), and the less triangular outline of the crown in posterior cheek teeth. The best match for the morphology of cheek teeth is with the poorly known *Neosqualodon*, from the Early Miocene of Italy (see Dal Piaz 1904; Fabiani 1949; Rothausen 1968; G. B. pers. obs.). However, MUSM 1980 differs from *Neosqualodon* in: its much larger size, with larger teeth; the styliform process of its jugal being markedly more robust; the posterior increase of the height of the mandible being less abrupt; its lower tooth count; incisors being not procumbent; and the number of accessory denticles in posterior cheek teeth being higher. Unfortunately, only

fragmentary ear bones were figured for one specimen of *Neosqualodon gastaldii* (Capellini 1881) and these ear bones could not be later found in the Bologna collection.

Another poorly known taxon is *Kekenodon onamata* Hector, 1881 from the Late Oligocene of New Zealand. It has been referred to archaeocetes (Kellogg 1936; Fordyce 2004; Clementz *et al.* 2014), or to basal toothed mysticetes (Fordyce and Muizon, 2001). The holotype of this taxon consists in several isolated teeth, a fragment of lower jaw, a tympanic and a periotic apparently belonging to the same individual. Among the seven teeth illustrated by Hector (1881), five of them are double-rooted, triangular, and bear up to four broad-based accessory denticles. In this respect, they resemble the posterior cheek teeth of *Inticetus* (C_8 to C_{11}). However, they distinctly differ from *Inticetus* in the following features: they are c. 30% larger, they have higher crowns, they do not present anteroposterior asymmetry (in lateral view), and their enamel apparently bears marked longitudinal ridges. The periotic figured by Hector resembles that of *Inticetus* in its large fovea epitubaria and the large ventrolateral tuberosity. The tympanic of *Kekenodon* essentially differs from that of *Inticetus* in its inner posterior prominence being wider than the outer prominence, while it is narrower in *Inticetus*. An undescribed, subcomplete skull recently attributed to *Kekenodon* sp. (Clementz *et al.* 2014) differs markedly from *Inticetus*, retaining many plesiomorphic features as compared to neocetes.

Among more fragmentarily known cetacean taxa, several isolated teeth display similarities with posterior cheek teeth of *Inticetus*. The species *Phococetus vasconum* is based on a single cheek tooth from the Burdigalian of Saint-Médart-en-Jalle, SW France (Delfortrie 1873; Kellogg 1936), a locality that also yielded the holotype of the squalodelphinid *Medocinia tetragorhina*, isolated odontocete teeth, and many fish remains (Delfortrie 1872, 1875; Priem 1914; Muizon 1988). With four mesial and five distal broad-based denticles, relatively smooth enamel, a mesiodistal length of the crown of 35.5 mm (as measured on a cast; Kellogg, 1936), and a long isthmus between mesial and distal roots, this tooth strongly resembles $C_{9\text{-}10}$ of MUSM 1980. The only difference we could note is the proportionally higher crown in *P. vasconum*. The latter was earlier proposed as an archaeocete (Kellogg 1936), possibly a kekenodontid archaeocete (Uhen 2008b; Fitzgerald 2010), and an enigmatic probable mysticete (Fordyce & Barnes 1994). Based on the morphological similarities and shared Burdigalian age, we think that systematic affinities of *P. vasconum* with *Inticetus* cannot be ruled out.

With its smooth enamel and relatively large accessory denticles, an isolated cheek tooth from Late Oligocene deposits of Australia identified as *Squalodon gambierensis*

(Glaessner 1955; Pledge & Rothausen 1977) displays similarities with posterior cheek teeth of MUSM 1980, for example C_8. This Australian tooth has been attributed to a kekenodontid archaeocete (Fordyce 2004; Fitzgerald 2010).

The marked dental similarities of the heterodont odontocete *Inticetus* with fragmentary remains tentatively attributed to non-odontocete cetaceans urges us to be cautious in the identification of isolated cetacean cheek teeth from the Oligocene-early Miocene. In several cases those may not be diagnostic at the suborder level (e.g., Geisler *et al.* in press).

In addition to the differences mentioned above at the level of ear bones and cheek teeth, *Inticetus* differs from the stem odontocete families Agorophiidae, Ashleycetidae, Mirocetidae, Simocetidae, and Xenorophidae (see Fordyce 2002; Uhen 2008b; Sanders & Geisler 2015; Geisler *et al.* 2014; Churchill *et al.* 2016; Godfrey *et al.* 2016) in: its larger size, the bony nares being located far posterior to level of antorbital notch and roughly vertical, the nasals being anteroposteriorly shorter, and the intertemporal constriction being most likely absent.

It further differs from Squalodontidae (see Kellogg 1923; Pilleri 1985; Muizon 1991; Dooley 2005) in: the absence of a pterygoid-maxilla contact on the palate, the styliform process of jugal being markedly more robust, the sutural contact of the jugal with the zygomatic process of the squamosal being longer, the presence of a deep notch separating the basioccipital crest from the falcate process of the exoccipital, the presence of a high rim around the internal acoustic meatus, and the incisors being not procumbent, with the crown being not fluted.

It further differs from Patriocetidae (see Dubrovo & Sanders 2000) in: its larger size, the bony nares being located far posterior to level of antorbital notch, the intertemporal constriction being most likely absent, and the zygomatic process of squamosal being proportionally shorter.

It further differs from *Waipatia* (see Fordyce 1994; Tanaka & Fordyce 2015a) in: its larger size, the styliform process of jugal being markedly more robust, the presence of a high rim around the internal acoustic meatus, the posterior increase of the height of the mandible being less abrupt; the incisors being not procumbent, and the presence of mesial denticles on upper and lower posterior cheek teeth.

It shares with *Papahu* (see Aguirre-Fernández & Fordyce 2014) the large fovea epitubaria with a correspondingly short anterior bullar facet (although more marked in MUSM 1980), but it differs from this homodont odontocete in: its larger size, the styliform

process of jugal being markedly more robust, an unconspicuous parabullary sulcus on the periotic, and the posterior increase of the height of the mandible being less abrupt.

Although *Inticetus* shares with *Prosqualodon davidis* a voluminous accessory ossicle, it further differs from *Prosqualodon* spp. (see Lydekker 1893; True 1909; Flynn 1948) in: the rostrum being proportionally longer, the posterior increase of the height of the mandible being less abrupt, a higher tooth count (compared to *P. davidis*), incisors being not procumbent, and the reduced ornamentation of the tooth crowns.

Phylogeny

To investigate the phylogenetic relationships of *Inticetus vertizi* we coded the specimen MUSM 1980 in the matrix of Tanaka & Fordyce (2016) (see list of morphological characters and character-taxon matrix as online Supplemental material). Note that as compared to this previous analysis, the Operational Taxonomic Unit OU 22125 is now named *Awamokoa tokarahi* (following Tanaka & Fordyce 2017). Four heuristic searches were performed using Paup 4.0 (Swofford 2001), with the protocetid *Georgiacetus vogtlensis* and the basilosaurid *Zygorhiza kochii* as outgroups, all characters treated as unordered, TBR branch swapping, and ACCTRAN optimization: (analysis 1) with equally weighted characters and no molecular constraint; (analysis 2) with down-weighted homoplastic characters, following the method of Goloboff (1993) with the constant k = 3 and no molecular constraint; (analysis 3) with equally weighted characters and with a backbone molecular constraint taken from the analysis of McGowen *et al.* (2009), as performed by Tanaka & Fordyce (2016), and (analysis 4) with down-weighted homoplastic characters and with a backbone molecular constraint.

Results

Analysis 1 resulted in 6480 most parsimonious trees with tree length 1828; CI 0.24; RI 0.64; the strict consensus is shown in Figure 26. Analysis 2 resulted in 9 most parsimonious trees with CI 0.24; RI 0.64; the strict consensus is partly shown in Figure 27A (without details for the clade Delphinida). Analysis 3 resulted in 135 most parsimonious trees with tree length 1914; CI 0.23; RI 0.62; the strict consensus is partly shown in Figure 27B. Analysis 4 resulted in 9 most parsimonious trees with CI 0.23; RI 0.62; the strict consensus is partly shown in Figure 27C.

Without any molecular constraint, analyses 1 and 2 identify the superfamily Platanistoidea as the most stemward crown odontocete clade, with Physeteroidea and

Ziphiidae forming a more crownward clade, itself sister-group to Delphinida. The content of Platanistoidea differs in these two analyses: in the analysis with equally weighted characters (analysis 1) it only includes *Squalodon*, *Prosqualodon*, a monophyletic Squalodelphinidae and a monophyletic Platanistidae, with *Inticetus* and a clade including *Otekaikea* and *Waipatia* being the last stem odontocete lineages to branch off, whereas in the analysis with down-weighted homoplastic characters (analysis 2) Platanistoidea also includes *Inticetus*, *Otekaikea* and *Waipatia*, and Squalodelphinidae is paraphyletic.

The molecular constraint (in analyses 3 and 4) places Physeteroidea as the first stem odontocete clade to branch off, followed by Platanistoidea and Ziphiidae. Here again the content of Platanistoidea differs if homoplastic characters are down-weighted or not. In the analysis with equally weighted characters (analysis 3), it only includes Platanistidae, a paraphyletic Squalodelphinidae, OU 22670 and *Papahu* sp. ZMT 73, with *Inticetus*, *Waipatia*, and *Otekaikea* forming a clade stemward to the successive branches of *Squalodon*, *Prosqualodon*, and Physeteroidea. In the analysis with down-weighted homoplastic characters (analysis 4), Platanistoidea makes a much larger clade, also including *Prosqualodon* + *Squalodon*, *Inticetus*, *Otekaikea*, and *Waipatia*, but not *Papahu* sp. ZMT 73.

Discussion

Down-weighting homoplastic characters has a profound impact on both the content of the superfamily Platanistoidea and the relationships of *Inticetus*; indeed, in the two analyses with equally weighted characters (analyses 1 and 3, without and with a molecular constraint), the clade Platanistoidea is less inclusive and *Inticetus* falls as a stem odontocete. Interestingly, the two analyses with down-weighted homoplastic characters (analyses 2 and 4) resulted in a larger clade Platanistoidea, which includes Platanistidae, Squalodelphinidae, *Inticetus*, *Otekaikea*, *Squalodon*, and *Waipatia*. The only difference between the two results is the position of *Prosqualodon*, which is either a stem taxon to Platanistoidea (analysis 2) or included in the Platanistoidea (analysis 4). Therefore, down-weighting homoplastic characters tends to tighten the clade Platanistoidea, and in both cases *Inticetus* is included in the superfamily.

A molecular constraint was applied for the two analyses performed by Tanaka & Fordyce (2016); those can thus only be compared to analyses 3 and 4. Interestingly, the inclusion of *Inticetus* in analysis 3 'attracts' *Otekaikea*, *Prosqualodon*, *Squalodon*, and *Waipatia* outside the Platanistoidea clade, and even outside the crown Odontoceti, a result that is not found in any of Tanaka & Fordyce's results. Nevertheless, *Prosqualodon*,

Squalodon, and in some cases *Waipatia* fell outside crown Odontoceti in several past phylogenetic analyses (e.g., Geisler *et al.* 2011, 2014; Aguirre-Fernández & Fordyce 2014; Tanaka & Fordyce 2014, 2015b; Sanders & Geisler 2015; Godfrey *et al.* 2016). Analysis 4 yields a general topology similar to the analysis of Tanaka & Fordyce (2016) with down-weighted homoplastic characters, meaning that in this case, reducing the impact of homoplastic characters tends to stabilize a topology when new taxa are added.

Based on our different results, there is no consensus about the phylogenetic relationships of *Inticetus*. It is either a stem odontocete more crownward than *Agorophius* and *Patriocetus* (in a separate lineage or in a clade with *Otekaikea* and *Waipatia*), or a crown odontocete branching off relatively early in a large Platanistoidea clade. In all our analyses, *Inticetus* is close to the node defining crown Odontoceti, and its most recurrent phylogenetic affinities are with (1) *Otekaikea* and *Waipatia*, either as sister-groups or as successive branches, and (2) *Squalodon*, as successive branches in two analyses (in one case with *Prosqualodon* as sister-group to *Squalodon*). However, *Inticetus* does not match any of the families, or genera from undetermined families, of Oligocene and Miocene odontocetes, displaying morphological features departing markedly from any other known taxon, including Squalodontidae and Waipatiidae. Because it differs strikingly from all the other heterodont odontocetes (see comparison above), and although the generally highly diagnostic facial region, including the vertex, is not optimally preserved in the holotype and only known specimen, we think that the diagnostic features of *Inticetus* should lead to the erection of a higher rank taxon, the new family Inticetidae.

Geological context, biostratigraphy and taphonomy

Geological context

The Meso-Cenozoic tectonics of the Peruvian margin was controlled by the oblique subduction of the oceanic Nazca-Farallon Plate beneath the continental South American Plate. This resulted in a composite transform-convergent margin characterized by normal and strike-slip faults that formed a number of extensional and pull apart basins along the western margin of Peru (e.g., Thornburg & Kulm 1981; León *et al.* 2008; Zúñiga-Rivero *et al.* 2010). The Cenozoic stratigraphy of the Pisco Basin in southern Peru consists of Eocene to Pliocene nearshore and shelf sediments that occur in repetitive successions and are separated by basin-wide, conglomerate-mantled unconformities (Dunbar *et al.* 1990; DeVries 1998). Based on the currently existing stratigraphic framework, the basin fill comprises the middle to upper

Eocene Paracas Formation, the uppermost Eocene to lower Oligocene Otuma Formation, the uppermost Oligocene to middle Miocene Chilcatay Formation, and the upper Miocene to Pliocene Pisco Formation (DeVries *et al.* 2006).

The Roca Negra locality is along the western side of the Ica River valley, where the Chilcatay Formation consists of two main sediment units separated by an intraformational unconformity. The lower unit includes a sub-horizontal package of medium- to fine-grained sandstones and siltstones that underlie and, locally, landward interfinger (from southwest to northeast) with a seaward-dipping clinoformed package of coarse-grained biocalcarenites. This lower unit is unconformably overlain by a fining-upward unit composed of basal sandstones gradually overlain by massive siltstones. An ash layer sampled in the fine-grained unit of the Chilcatay Formation, just 1 m below the erosional contact with the overlying Pisco Formation, yielded a $^{40}Ar/^{39}Ar$ age of 17.99 ± 0.10 Ma (Di Celma *et al.* 2017).

Biostratigraphy

The Chilcatay sedimentary succession exposed in the locality of MUSM 1980 (Roca Negra) is part of the sub-horizontal package of sandstones and siltstones occurring in the lower portion of the lower unit. Most of the samples recovered for biostratigraphic analysis along the measured section had a lithogenic composition. Sample PN2 (see Fig. 2) contained a well preserved siliceous assemblage (see Appendix 1). Silicoflagellates were rare but yielded a diverse assemblage, represented, in order of abundance, by *Naviculopsis obtusarca*, *Distephanopsis crux* subsp. *scutulata*, *Corbisema triacantha*, *N. ponticula* subsp. *ponticula*, *N. obtusarca* var. *acicula* and *Naviculopsis* sp. 2 (described by Cisielsky 1991 from the Early Miocene of the sub-Antarctic South Atlantic). Accordingly, this assemblage is assigned to the *Naviculopsis ponticula* zone of Bukry (1981), correlated by Bukry (1982) to the coccolith *Sphenolithus belemnos* Zone at DSDP Site 495 offshore Guatemala, that, in turn, has been dated between 19 and 18 Ma (Bukry, 1982), early Burdigalian. Bukry (1985) described this biozone across the equatorial Pacific and showed that it is dominated sequentially by *N. obtusarca*, *N. contraria*, and *N. ponticula* var. *spinosa*. In our sample, given the dominance of the former and the absence of the latter two species, we can speculate that it is located in the lower part of the *N. ponticula* biozone. Macharé *et al.* (1998) indicated the presence of *N. ponticula spinosa* in one sample (84407) at the Pampa Chilcatay section, along with a diatom assemblage including *Triceratium pileus*, *Thalassiosira fraga*, and *Th. spinosa*; according to Barron (1985), this diatom assemblage indicates an age of 18.8 to 17.9 Ma. *N. ponticula* is otherwise reported from the eastern Equatorial Pacific (Engel & McCartney 1990), the eastern

Equatorial Atlantic (Schellpeper & Watkins 1998), and outcrops of the temperate North Atlantic (Wetmore & Andrews 1991).

Taphonomy

Although the fossil skeleton MUSM 1980 was only partly articulated, all the bones were found associated, roughly near their original anatomical position, and with the axial skeleton (both the forelimbs are lost) forming on the whole an arc (Fig. 28). The disarticulation mainly concerns the ribcage (thoracic vertebrae, ribs, and sternal bones). Except for slight displacement due to wind for exposed bones included in soft, uncemented sediment, most disarticulation probably occurred before the burial of the skeleton and could be due to: 1) collapse of the ribcage after decomposition of soft tissues, 2) explosion resulting from the accumulation of gases generated during the decay of the carcass, 3) water currents on the sea bottom, or 4) scavenging by sharks and other marine vertebrates. This last possibility is strongly supported by the finding on the one side of three isolated shark teeth near the bones of the odontocete and, on the other side, of shark bite marks along the rostrum of the cranium and along the left mandible. Discovered near the sternum and near the anteriormost lumbar vertebrae, the shark teeth belong to three distinct species already recorded in the late Miocene strata of the Pisco Formation: *Cosmopolitodus hastalis, Galeocerdo aduncus*, and *Pysogaleous contortus*, (Muizon & DeVries 1985; Collareta *et al.* 2017; Landini *et al.* 2017). Considering the trophic spectrum of the extant relatives of these sharks, and/or of other similar extant sharks (Klymley 1994; Long & Jones 1996; Heithaus 2001; Curtis *et al.* 2006), it is reasonable to suggest that these teeth indicate the partial consumption of the carcass by sharks of these three species. Such an occurrence is relatively common during the excavation of fossil cetacean skeletons and it was also well documented for a whale skeleton from the Pisco Formation (Takakuwa 2014).

Most of the bite marks are observed in the left dorsolateral side of the rostrum. They consist in some pseudo-parallel incisions about 2 cm long. These shallow grooves lacking serrated margins could correspond to scraping marks caused by one or more sharks biting the carcass of the odontocete. Scavenging, rather than active predation, is supported by the fact that the incisions are not deep, in relatively small number, and located in a portion of the skeleton (skull and mandibles) usually not damaged during a shark attack. Indeed, data about the well-documented feeding behaviour of the extant white shark *Carcharodon carcharias* indicate that sharks usually do not target the head region of dolphins in order to avoid sonar detection (Long & Jones 1996). For this reason a direct predation, conceivable for other fossil

odontocetes with several deep shark bites in the ribcage region (Cigala Fugosi 1992, Bianucci *et al.* 2010), cannot be proposed for the fossil examined here. Scavenging by sharks could also explain the absence of both forelimbs, possibly removed when the carcass was still floating, or after it sank to the seafloor (Shäfer 1972; Bianucci & Gingerich 2011). Re-floating of the carcass, due to a buildup of gases during initial decomposition (Shäfer 1972), did most likely not occur, or for only a short time, before it sank to the bottom, considering the preservation of the mandibles firmly articulated to the cranium, of most of the teeth inside their alveoli, and of the last caudal vertebrae.

General discussion and conclusions

With such unusual tooth morphology, the feeding ecology of *Inticetus* is worth briefly discussing. First, among heterodont odontocetes the general outline of the long and robust rostrum is most similar to *Squalodon*, contrasting with the much shorter rostrum of *Prosqualodon* and the more slender rostrum of e.g. *Waipatia*. Combined with strong, but not procumbent, conical anterior teeth, this condition suggests the ability to grasp relatively large prey with the incisors, canines, and anterior cheek teeth, as proposed for at least part of the basilosaurids (Uhen 2004; Snively *et al.* 2015). However, contrasting with basilosaurids (Uhen 2004; Fahlke *et al.* 2013), the absence of conspicuous attritional tooth wear facets in cheek teeth may indicate only a limited use of the posterior dentition for processing food (namely cutting or tearing larger prey in smaller pieces), a hypothesis further supported by the highly reduced ornamentation of tooth crowns. Furthermore, the enlarged, broad-based accessory denticles displayed by the closely spaced posterior cheek teeth leads to a better closure of the lateral wall of the posterior buccal cavity. Differing from most other heterodont odontocetes, such a condition may correspond to higher suction-feeding abilities, with rigid lateral walls of the cavity allowing the production of higher intraoral pressure during suction and with broad dental crowns allowing the retention of food items when water is expelled laterally from the cavity during the recovery phase (see Werth 2006). A similar conclusion has been experimentally confirmed for pinnipeds showing enlarged accessory denticles in cheek teeth (Hocking *et al.* 2013).

In addition to its dental morphology, *Inticetus* differs from many other Late Oligocene - Early Miocene odontocetes in its larger body size; except from the larger, homodont physeteroids *Diaphorocetus poucheti* and *Idiorophus patagonicus* (Moreno 1892; Lydekker 1894), *Inticetus* is only in the same size category as *Phoberodon arctirostris*, *Prosqualodon*

spp. and the homodont *Macrodelphinus kelloggi* (Lydekker 1893; Flynn 1948; Cabrera 1926; Wilson 1935).

Combining the skull morphology, dental features, and size of *Inticetus*, this heterodont odontocete further increases the morphological disparity of Late Oligocene - Early Miocene odontocetes; it most likely occupied a relatively specific ecological niche.

From a phylogenetic viewpoint, the relationships of *Inticetus* are not fully resolved, this new taxon being either a stem odontocete or an early diverging platanistoid. The addition of other Late Oligocene - Early Miocene heterodont odontocetes to the analysed sample and the reassessment of *Prosqualodon* spp. and the family Squalodontidae may prove useful to further characterize the stem-to-crown odontocete transition.

Finally, from a taxonomic perspective, the description of an unusual morphotype of odontocete cheek teeth, sharing similarities with the dentition of a few other, non-odontocete fossil cetaceans, urges the need for caution in the identification of isolated cetacean teeth, even at the suborder level.

Supplemental material

Supplemental material for the phylogenetic analysis, including the character-taxon matrix and the constraint tree based on molecular analysis is available online at doi: ...

Acknowledgements

We wish to warmly thank A. Altamirano-Sierra, E. Díaz, and K. Post for their help during fieldwork, W. Aguirre for the preparation of the skull and postcranial remains, R. Salas-Gismondi and R. Varas-Malca for providing access to the MUSM collection and for facilitating our work there, W. Miseur for the photographs of ear bones, and the reviewers B. L. Beatty and R. E. Fordyce, as well as the editors, for their constructive, useful comments. This research was supported by funding from the Muséum national d'Histoire naturelle, Paris (Action Transversale "Biodiversité actuelle et fossile" 2011) to C.M. and O.L., a grant of the Italian Ministero dell'Istruzione dell'Università e della Ricerca (PRIN Project 2012YJSBMK) to C.D.C., E.M. and G.B., and a National Geographic Society Committee for Research Exploration grant (9410–13) to G.B.

References

Abel, O. 1901. Les dauphins longirostres du Boldérien (Miocène supérieur) des environs d'Anvers. I. *Mémoires du Musée Royal d'Histoire Naturelle de Belgique*, **1**, 1-95.

Aguirre-Fernández, G. & Fordyce, R. E. 2014. *Papahu taitapu*, gen. et sp. nov., an early Miocene stem odontocete (Cetacea) from New Zealand. *Journal of Vertebrate Paleontology*, **34**, 195-210.

Armfield, B. A., Zheng, Z., Bajpai, S., Vinyard, C. J. & Thewissen, J. M. G. 2013. Development and evolution of the unique cetacean dentition. *PeerJ*, **1**, e24.

Barron, J. A. 1985. Miocene to Holocene planktic diatom stratigraphy. Pp. 413-456 in H. M. Bolli, J. B. Saunders & K. Perch-Nielsen (eds.) *Plankton Stratigraphy*. Cambridge University Press, UK.

Bianucci, G. & Gingerich, P. D. 2011. *Aegyptocetus tarfa*, n. gen. et sp. (Mammalia, Cetacea), from the middle Eocene of Egypt: clinorhynchy, olfaction, and hearing in a protocetid whale. *Journal of Vertebrate Paleontolology*, **31**, 1173-1188.

Bianucci, G. & Landini, W. 2006. Killer sperm whale: a new basal physeteroid (Mammalia, Cetacea) from the Late Miocene of Italy. *Zoological Journal of the Linnean Society*, **148**, 103-131.

Bianucci, G., Lambert, O. & Post, K. 2010. High concentration of long-snouted beaked whales (genus *Messapicetus*) from the Miocene of Peru. *Palaeontology*, **53**, 1077-1098.

Bianucci, G., Sorce, B., Storai, T. & Landini, W. 2010. Killing in the Pliocene: shark attack on a dolphin from Italy. *Palaeontology*, **53**, 457-470.

Bianucci, G., Urbina, M. & Lambert, O. 2015. A new record of *Notocetus vanbenedeni* (Squalodelphinidae, Odontoceti, Cetacea) from the early Miocene of Peru. *Comptes Rendus Palevol*, **14**, 5-13.

Bianucci, G., Di Celma, C., Landini, W., Post, K., Tinelli, C., de Muizon, C., Gariboldi, K., Malinverno, E., Cantalamessa, G., Gioncada, A., Collareta, A., Salas-Gismondi, R., Varas-Malca, R., Urbina, M. & Lambert, O. 2016a. Distribution of fossil marine vertebrates in Cerro Colorado, the type locality of the giant raptorial sperm whale *Livyatan melvillei* (Miocene, Pisco Formation, Peru). *Journal of Maps*, **12**, 543-557.

Bianucci, G., Di Celma, C., Urbina, M. & Lambert, O. 2016b. New beaked whales from the late Miocene of Peru and evidence for convergent evolution in stem and crown Ziphiidae (Cetacea, Odontoceti). *PeerJ*, **4**, e2479.

Brisson, M.-J. 1762. *Regnum Animale in classes IX distributum, sine synopsis methodica*. Theodorum Haak, Paris, 296 pp.

Buchholtz, E. A. 2001. Vertebral osteology and swimming style in living and fossil whales (Order Cetacea). *Journal of Zoology*, **253**, 175-190.

Buchholtz, E. A. & Schur, S. A. 2004. Vertebral osteology in Delphinidae (Cetacea). *Zoological Journal of the Linnean Society*, **140**, 383-401.

Bukry, D. 1978. Cenozoic coccolith, silicoflagellate, and diatom stratigraphy, Deep Sea Drilling Project Leg 44. *Initial Reports, DSDP*, **44**, 807-863.

Bukry, D. 1981. Synthesis of silicoflagellate stratigraphy for Maastrichtian to Quaternary marine sediments. Pp. 433–444 in T. E. Warme, R. C. Douglas & E. L. Winterer (eds.) *The deep sea drilling project: a decade of progress.* Special Publication - SEPM, 32.

Bukry, D. 1982. Cenozoic silicoflagellates from offshore Guatemala, Deep Sea Drilling Project site 495. *Initial Reports, DSDP*, **67**, 425-445.

Bukry, D. 1985. Tropical Pacific silicoflagellate zonation and paleotemperature trends of the late Cenozoic. *Initial Reports, DSDP*, **85**, 477-497.

Cabrera, A. 1926. Cetaceos fosiles del Museo de La Plata. *Revista del Museo de La Plata*, **29**, 363-411.

Capellini, G. 1881. Avanzi di Squalodonte nella mollassa marnosa miocenica del Bolognese. *Memorie della Accademia delle Scienze dell'Istituto di Bologna, ser. 4*, **2**, 413-419.

Churchill, M., Martinez-Caceres, M., de Muizon, C., Mnieckowski, J. & Geisler, J. H. 2016. The origin of high-frequency hearing in whales. *Current Biology*, **26**, 2144-2149.

Ciesielski, P.F. 1991. Biostratigraphy of diverse silicoflagellate assemblages from the early Paleocene to early Miocene of holes 698A, 700B, 702B, AND 703A: Subantarctic South Atlantic. *Proceedings of the Ocean Drilling Program, Scientific Results*, **114**, 49-96.

Cigala Fulgosi, F. 1990. Predation (or possible scavenging) by a great white shark on an extinct species of bottlenosed dolphin in the Italian Pliocene. *Tertiary Research*, **12**, 17–36.

Clementz, M. T., Fordyce, R. E., Peek, S. L. & Fox, D. L. 2014. Ancient marine isoscapes and isotopic evidence of bulk-feeding by Oligocene cetaceans. *Palaeogeography, Palaeoclimatology, Palaeoecology*, **400**, 28-40.

Collareta, A., Landini, W., Chacaltana, C., Valdivia, W., Altamirano-Sierra, A., Di Celma, C., Urbina, M. & Bianucci, G. 2017. A well preserved skeleton of the fossil shark *Cosmopolitodus hastalis* from the late Miocene of Peru, featuring fish remains as fossilized stomach contents. *Rivista Italiana di Paleontologia e Stratigrafia*, **123**, 11-22.

Cotten, P. B., Piscitelli, M. A., McLellan, W. A., Rommel, S. A., Dearolf, J. L. & Pabst, D. A.. 2008. The gross morphology and histochemistry of respiratory muscles in bottlenose dolphins, *Tursiops truncatus*. *Journal of Morphology*, **269**, 1520-1538.

Curtis, T. H., Kelly, J. T., Menard, K. L., Laroche, R. K., Jones, R. E. & Klimley, A. P. 2006. Observations on the behavior of white sharks scavenging from a whale carcass at Point Reyes, California. *California Fish and Game*, **92**, 113-124.

Dal Piaz, G. 1904. *Neosqualodon*, nuovo genere della famiglia degli Squalodontidi. *Mémoires de la Société Paléontologique Suisse*, **31**, 1-19.

Delfortrie, E. 1872. Les phoques du falun aquitanien. *Actes de la Société Linnéenne de Bordeaux*, **28**, 383-386.

Delfortrie, E. 1873. Un Zeuglodon dans les faluns du sud-ouest de la France. *Journal de Zoologie*, **9**, 113-117.

Delfortrie, E. 1875. Un dauphin d'espèce nouvelle dans les faluns du Sud-Ouest. *Actes de la Société Linnéenne de Bordeaux*, **30**, 3-7.

Desikachary, T. V. & Prema, P. 1996. Silicoflagellates (Dictyochophyceae). *Bibliotheca Phycologica*, **100**, 1–298

DeVries, T. J. 1998. Oligocene deposition and Cenozoic sequence boundaries in the Pisco Basin (Peru). *Journal of South American Earth Sciences*, **11**, 217-231.

DeVries, T. J. 2001. Molluscan evidence for an Oligocene-Miocene age of 'Paracas' beds in Southern Peru. *Boletín de la Sociedad Geológica del Perú*, 92, 57-65.

DeVries, T. J., Navarez, Y., Sanfilippo, A., Malumian, N. &Tapia, P. 2006. New microfossil evidence for a late Eocene age of the Otuma Formation (Southern Peru). *XIII Congreso Peruano de Geología, Lima, Peru*, 615-618.

Di Celma, C., Malinverno, E., Bosio, G., Collareta, A., Gariboldi, K., Gioncada, A., Molli, G., Basso, D., Varas-Malca, R., Pierantoni, P.P., Villa, I.M., Lambert, O., Landini, W., Sarti, G., Cantalamessa, G., Urbina, M. & Bianucci, G. 2017.

Allostratigraphy and palaeontology of the upper Miocene Pisco Formation along the western side of the lower Ica Valley (Ica Desert, Peru). *Rivista Italiana di Paleontologia e Stratigrafia*, **123**, 255-273.

Dooley, A. C., Jr. 2005. A new species of *Squalodon* (Mammalia, Cetacea) from the Middle Miocene of Virginia. *Virginia Museum of Natural History Memoir*, **8**, 1-43.

Dubrovo, I. A. & Sanders, A. E. 2000. A new species of *Patriocetus* (Mammalia, Cetacea) from the late Oligocene of Kazakhstan. *Journal of Vertebrate Paleontology*, **20**, 577-590.

Dunbar, R. B., Marty, R. C. & Baker, P. A. 1990. Cenozoic marine sedimentation in the Sechura and Pisco basins, Peru. *Palaeogeography, Palaeoclimatology, Palaeoecology*, **77**, 235-261.

Engel, R. & McCartney, K. 1990. Silicoflagellates recovered from Deep Sea, ODP Leg 199 site 1219, east Equatorial Pacific. *Proceedings of the Ocean Drilling Program, Scientific Results*, **199**, 1-29.

Fahlke, J. M., Bastl, K. A., Semprebon, G. M. & Gingerich, P. D. 2013. Paleoecology of archaeocete whales throughout the Eocene: Dietary adaptations revealed by microwear analysis. *Palaeogeography, Palaeoclimatology, Palaeoecology*, **386**, 690-701.

Fitzgerald, E. M. G. 2010. The morphology and systematics of *Mammalodon colliveri* (Cetacea: Mysticeti), a toothed mysticete from the Oligocene of Australia. *Zoological Journal of the Linnean Society*, **158**, 367-476.

Flower, W. H. 1867. Description of the skeleton of *Inia geoffrensis* and the skull of *Pontoporia blainvillii*, with remarks on the systematic position of these animals in the Order Cetacea. *Transactions of the Zoological Society of London*, **6**, 87-116.

Flynn, T. T. 1948. Description of *Prosqualodon davidi* Flynn: A fossil cetacean from Tasmania. *Transactions of the Zoological Society of London*, **26**, 153-197.

Fordyce, R. E. 1981. Systematics of the odontocete whale *Agorophius pygmaeus* and the family Agorophiidae (Mammalia: Cetacea). *Journal of Paleontology*, **55**, 1028-1045.

Fordyce, R. E. 1982. Dental anomaly in a fossil squalodont dolphin from New Zealand, and the evolution of polydonty in whales. *New Zealand Journal of Zoology*, **9**, 419-426.

Fordyce, R. E. 1994. *Waipatia maerewhenua*, new genus and new species (Waipatiidae, new family), an archaic late Oligocene dolphin from New Zealand. Pp. 147-178 in A. Berta & T. A. Deméré (eds.) *Contributions in marine mammal paleontology honoring Frank C. Whitmore, Jr*. Proceedings of the San Diego Society of Natural History, 29.

Fordyce, R. E. 2002. *Simocetus rayi* (Odontoceti: Simocetidae) (new species, new genus, new family), a bizarre new archaic Oligocene dolphin from the eastern North Pacific. *Smithsonian Contributions to Paleobiology* 93: 185-222.

Fordyce, R. E. 2004. The transition from Archaeoceti to Neoceti: Oligocene archaeocetes in the southwest Pacific. *Journal of Vertebrate Paleontology* 24 (suppl. to 3): 59A.

Fordyce, R. E. & Barnes, L. G. 1994. The evolutionary history of whales and dolphins. *Annual Review of Earth and Planetary Science* 22: 419-455.

Fordyce, R. E. & Muizon, C., de. 2001. Evolutionary history of cetaceans: a review. Pp. 169-233 in J.-M. Mazin & V. de Buffrénil (eds.) *Secondary adaptation of tetrapods to life in water*. Verlag Dr. Friedrich Pfeil, München.

Galatius, A. & Kinze, C. C. 2003. Ankylosis patterns in the postcranial skeleton and hyoid bones of the harbour porpoise (*Phocoena phocoena*) in the Baltic and North Sea. *Canadian Journal of Zoology*, **81**, 1851-1861.

Geisler, J. H., Sanders, A. E. & Luo, Z.-X. 2009. A new protocetid whale (Cetacea: Archaeoceti) from the late middle Eocene of South Carolina. *American Museum Novitates*, **3480**, 1-65.

Geisler, J. H., McGowen, M. R., Yang, G. & Gatesy, J. 2011. A supermatrix analysis of genomic, morphological, and paleontological data for crown Cetacea. *BMC Evolutionary Biology*, **11**, 1-22.

Geisler, J. H., Colbert, M. W. & Carew, J. L. 2014. A new fossil species supports an early origin for toothed whale echolocation. *Nature*, **508**, 383-386.

Geisler, J. H., Boessenecker, R. W., Brown, M. & Beatty, B. L. In press. The origin of filter feeding in whales. *Current Biology*. doi: 10.1016/j.cub.2017.06.003

Glaessner, M. 1955. Pelagic fossils (*Aturia*, penguins, whales) from the Tertiary of South Australia. *Records of the South Australian Museum*, **11**, 353-372.

Godfrey, S. J., Uhen, M. D., Osborne, J. E. & Edwards, L. E. 2016. A new specimen of *Agorophius pygmaeus* (Agorophiidae, Odontoceti, Cetacea) from the early Oligocene Ashley Formation of South Carolina, USA. *Journal of Paleontology*, **90**, 154-169.

Goloboff, P. A. 1993. Estimating character weights during tree search. *Cladistics*, **9**, 83-91.

Hanna, G. D. 1931. Diatoms and silicoflagellates of the Kreyenhagen shale. *California Division of Mines Report*, **27**, 187-201.

Hector, J. 1881. Notes on New Zealand Cetacea, recent and fossil. *Transactions and Proceedings of the New Zealand Institute*, **13**, 434-437.

Heithaus, M. R. 2001. Predator-prey and competitive interactions between sharks and dolphins: a review. *Journal of Zoology*, **253**, 53-68.

Heyning, J. E. 1997. Sperm whale phylogeny revisited: analysis of the morphological evidence. *Marine Mammal Science*, **13**, 596-613.

Hocking, D. P., Evans, A. R. & Fitzgerald, E. M. G. 2013. Leopard seals (*Hydrurga leptonyx*) use suction and filter feeding when hunting small prey underwater. *Polar Biology*, **36**, 211-222.

Ichishima, H. 2016. The ethmoid and presphenoid of cetaceans. *Journal of Morphology*, **277**, 1661-1674.

Kellogg, R. 1923. Description of two squalodonts recently discovered in the Calvert Cliffs, Maryland; and notes on the shark-toothed dolphins. *Proceedings of the United States National Museum*, **62**(6), 1-69.

Kellogg, R. 1936. A review of the Archaeoceti. *Carnegie Institute of Washington Publication*, **482**, 1-366.

Klimley, A. P. 1994. The predatory behavior of the white shark. *American Scientist*, **82**, 122–133.

Lambert, O. 2005. Phylogenetic affinities of the long-snouted dolphin *Eurhinodelphis* (Cetacea, Odontoceti) from the Miocene of Antwerp. *Palaeontology*, **48**, 653-679.

Lambert, O., Bianucci, G. & Urbina, M. 2014. *Huaridelphis raimondii*, a new early Miocene Squalodelphinidae (Cetacea, Odontoceti) from the Chilcatay Formation, Peru. *Journal of Vertebrate Paleontology*, **34**, 987-1004.

Lambert, O., Muizon, C., de & Bianucci, G. 2015. A new archaic homodont toothed whale (Mammalia, Cetacea, Odontoceti) from the early Miocene of Peru. *Geodiversitas*, **37**, 79-108.

Lambert, O., Bianucci, G. & Muizon, C., de. 2016. Macroraptorial sperm whales (Cetacea, Odontoceti, Physeteroidea) from the Miocene of Peru. *Zoological Journal of the Linnean Society*. doi: 10.1111/zoj.12456

Lambert, O., Bianucci, G., Urbina, M. & Geisler, J. H. 2017. A new inioid (Cetacea, Odontoceti, Delphinida) from the Miocene of Peru and the origin of modern dolphin and porpoise families. *Zoological Journal of the Linnean Society*, **179**, 919-946.

Landini, W., Altamirano-Sierra, A., Collareta, A., Di Celma, C., Urbina, M. & Bianucci, G. 2017. The late Miocene elasmobranch assemblage from Cerro Colorado (Pisco Formation, Peru). *Journal of South American Earth Sciences*, **73**, 168-190.

León, W., Aleman, A., Torres, V., Rosell, W. & De La Cruz, O. 2008. Estratigrafía, sedimentología y evolución tectónica de la cuenca Pisco Oriental. *Boletín INGEMMET*, **27**, 1-144.

Long, D. J. & Jones, R. E. 1996. White shark predation and scavenging on cetaceans in the eastern North Pacific Ocean. Pp. 293-307 in A. P. Klimley & D. G. Ainley (eds.) *Great white sharks: the biology of* Carcharodon carcharias. Academic Press, San Diego.

Luo, Z.-X. & Gingerich, P. D. 1999. Terrestrial Mesonychia to aquatic Cetacea: transformation of the basicranium and evolution of hearing in whales. *University of Michigan Papers on Paleontology*, **31**, 1-98.

Lydekker, R. 1893. Contribution to the knowledge of the fossil vertebrates of Argentina. Part II. Cetacean skulls from Patagonia. *Anales del Museo de La Plata*, **1893**, 1-14.

MacPhee, R. D. 1981. Auditory regions of primates and eutherian insectivores. *Contributions to Primatology*, **18**, 1-282.

Macharé, J., DeVries, T., Barron, J. & Fourtanier, E. 1988, Oligo-Miocene transgression along the Pacifie margin of South America: new paleontological and geological evidence from the Pisco basin (Peru). *Géodynamique*, **3**, 25-37.

Martínez-Cáceres, M., Lambert, O. & Muizon, C. de. 2017. The anatomy and phylogenetic affinities of *Cynthiacetus peruvianus*, a large *Dorudon*-like basilosaurid (Cetacea, Mammalia) from the late Eocene of Peru. *Geodiversitas*, **39**, 7-163.

Marx, F. G., Lambert, O. & Uhen, M. D. 2016. *Cetacean paleobiology*. John Wiley & Sons, Chichester, UK, 319 pp.

McGowen, M. R., Spaulding, M. & Gatesy, J. 2009. Divergence date estimation and a comprehensive molecular tree of extant cetaceans. *Molecular Phylogenetics and Evolution*, **53**, 891-906.

Mead, J. G. & Fordyce, R. E. 2009. The therian skull: a lexicon with emphasis on the odontocetes. *Smithsonian Contributions to Zoology*, **627**, 1-248.

Moreno, F. P. 1892. Noticias sobre algunos cetáceos fósiles y actuales de la República Argentina. *Revista del Museo de La Plata*, **3**, 383-400.

Muizon, C., de. 1985. Nouvelles données sur le diphylétisme des Dauphins de rivière (Odontoceti, Cetacea, Mammalia). *Comptes Rendus de l'Académie des Sciences, Paris*, **301**, 359-361.

Muizon, C., de. 1987. The affinities of *Notocetus vanbenedeni*, an Early Miocene platanistoid (Cetacea Mammalia) from Patagonia, southern Argentina. *American Museum Novitates*, **2904**, 1-27.

Muizon, C., de. 1988. Le polyphylétisme des Acrodelphidae, odontocètes longirostres du Miocène européen. *Bulletin du Muséum National d'Histoire Naturelle, Paris*, **10**, 31-88.

Muizon, C., de. 1991. A new Ziphiidae (Cetacea) from the Early Miocene of Washington State (USA) and phylogenetic analysis of the major groups of odontocetes. *Bulletin du Muséum National d'Histoire Naturelle, Paris, series 4*, **12**, 279-326.

Muizon, C., de. 1994. Are the squalodonts related to the platanistoids? Pp. 135-146 in A. Berta & T. Deméré (eds.) *Contributions in marine mammal paleontology honoring Frank Whitmore Jr*. Proceedings of the San Diego Society of Natural History, 29.

Muizon, C., de & DeVries, T. J. 1985. Geology and paleontology of late Cenozoic marine deposits in the Sacaco area (Peru). *Geologische Rundschau*, **74**, 547-563.

Muizon, C., de, Billet, G., Argot, C., Ladevèze, S. & Goussard, F. 2015. *Alcidedorbignya inopinata*, a basal pantodont (Placentalia, Mammalia) from the early Palaeocene of Bolivia: anatomy, phylogeny and palaeobiology. *Geodiversitas*, **37**, 397-634.

O'Leary, M. A. 2010. An anatomical and phylogenetic study of the osteology of the petrosal of extant and extinct artiodactylans (Mammalia) and relatives. *Bulletin of the American Museum of Natural History*, **335**, 1-206.

Park, T., Fitzgerald, E. M. G. & Evans, A. R. 2016. Ultrasonic hearing and echolocation in the earliest toothed whales. *Biology Letters*, **12**, 20160060.

Pilleri, G. 1985. The Miocene Cetacea of the Belluno sandstones (eastern southern Alps). *Memorie di Scienze Geologiche*, **36**, 1-87.

Pledge, N. S. & Rothausen, K. 1977. *Metasqualodon harwoodi* (Sanger, 1881) - a redescription. *Records of the South Australian Museum*, **17**, 285-297.

Priem, M. F. 1914. Sur les poissons fossiles des terrains tertiaires supérieurs du Sud-Ouest de la France. *Bulletin de la Société Géologique de France*, **14**, 118-131.

Pyenson, N. D. & Sponberg, S. N. 2011. Reconstructing body size in extinct crown Cetacea (Neoceti) using allometry, phylogenetic methods and tests from the fossil record. *Journal of Mammalian Evolution*, **18**, 269-288.

Rothausen, K. 1968. Die systematische Stellung der europäischen Squalodontidae (Odontoceti, Mamm.). *Palaeontologische Zeischrift*, **42**, 83-104.

Sanders, A. E. & Geisler, J. H. 2015. A new basal odontocete from the upper Rupelian of South Carolina, USA, with contributions to the systematics of *Xenorophus* and *Mirocetus* (Mammalia, Cetacea). *Journal of Vertebrate Paleontology*, **35**, e890107.

Schäfer, W. 1972. *Ecology and palaeoecology of marine environments*. The University of Chicago Press, Chicago, 568 pp.

Schellpeper, M. E. & Watkins, D. K. 1998. Oligocene to early Miocene silicoflagellates from the Ivorian Basin, eastern equatorial Atlantic, site 959. *Proceedings of the Ocean Drilling Program, Scientific Results*, 159, 493-508.

Snively, E., Fahlke, J. M. & Welsh, R. C. 2015. Bone-breaking bite force of *Basilosaurus isis* (Mammalia, Cetacea) from the Late Eocene of Egypt estimated by Finite Element Analysis. *PLoS ONE*, **10**, e0118380.

Swofford, D. L. 2001. *PAUP*. Phylogenetic analysis using parsimony (*and other methods). Version 4b10*. Sinauer Associates, Sunderland, Massachusetts.

Takakuwa, Y. 2014. A dense occurrence of teeth of fossil "mako" shark ("*Isurus" hastalis*: Chondrichthyes, Lamniformes), associated with a balaenopterid-whale skeleton of the late Miocene Pisco Formation, Peru, South America. *Bulletin of the Gunma Museum of Natural History*, **18**, 77-86.

Tanaka, Y. & Fordyce, R. E. 2014. Fossil dolphin *Otekaikea marplesi* (latest Oligocene, New Zealand) expands the morphological and taxonomic diversity of Oligocene cetaceans. *PLoS ONE*, **9**, e107972.

Tanaka, Y. & Fordyce, R. E. 2015a. Historically significant late Oligocene dolphin *Microcetus hectori* Benham 1935: a new species of *Waipatia* (Platanistoidea). *Journal of the Royal Society of New Zealand*, **45**, 135-150.

Tanaka, Y. & Fordyce, R. E. 2015b. A new Oligo-Miocene dolphin from New Zealand: *Otekaikea huata* expands diversity of the early Platanistoidea. *Palaeontologia Electronica*, **18.2.23A**, 1-71.

Tanaka, Y. & Fordyce, R. E. 2016. *Papahu*-like fossil dolphin from Kaikoura, New Zealand, helps to fill the Early Miocene gap in the history of Odontoceti. *New Zealand Journal of Geology and Geophysics*, **59**, 551-567.

Tanaka, Y. & Fordyce, R. E. 2017. *Awamokoa tokarahi*, a new basal dolphin in the Platanistoidea (late Oligocene, New Zealand). *Journal of Systematic Palaeontology*, **15**, 365-386.

Thornburg T. M. & Kulm L. D. 1981. Sedimentary basins of the Peru continental margin: Structure, stratigraphy, and Cenozoic tectonics from 6°S to 16°S latitude. Pp. 393-422

in: L. D. Kulm, J. Dymond, E. J. Dasch & D. M. Hussong (eds.) *Nazca plate: Crustal formation and Andean convergence*. Geological Society of America, Memoir 154, Boulder, CO.

True, F.W. 1909. A new genus of fossil cetaceans from Santa Cruz Territory, Patagonia; and description of a mandible and vertebrae of *Prosqualodon*. *Smithsonian Miscellaneous Collections*, **52**, 441-456.

Uhen, M. D. 2004. Form, function, and anatomy of *Dorudon atrox* (Mammalia, Cetacea): an archaeocete from the middle to late Eocene of Egypt. *University of Michigan Papers on Paleontology*, **34**, 1-222.

Uhen, M. D. 2008a. New protocetid whales from Alabama and Mississippi, and a new cetacean clade, Pelagiceti. *Journal of Vertebrate Paleontology*, **28**, 589-593.

Uhen, M. D. 2008b. A new *Xenorophus*-like odontocete cetacean from the Oligocene of North Carolina and a discussion of the basal odontocete radiation. *Journal of Systematic Palaeontology*, **6**, 433-452.

Uhen, M. D. 2009. Dental mophology, evolution of. Pp. 302-307 in W. F. Perrin, B. Würsig & J. G. M. Thewissen (eds.) *Encyclopedia of Marine Mammals, second edition*. Academic Press, San Diego.

Wells, R. S. & Scott, M. D. 1999. Bottlenose dolphin *Tursiops truncatus* (Montagu, 1821). Pp. 137-182 in S. H. Ridgway & R. Harrison (eds.) *Handbook of marine mammals, vol. 6: The second book of dolphins and the porpoises*. Academic Press, London.

Werth, A. J. 2006. Mandibular and dental variation and the evolution of suction feeding in Odontoceti. *Journal of Mammalogy*, **87**, 579-588.

Wetmore, K. L. & Andrews, G. W. 1991. Silicoflagellate and diatom biostratigraphy in successive Burdigalian transgressions, middle Atlantic coastal plain. *Micropaleontology*, **36**, 283-295.

Whitmore, F. C., Jr. & Sanders, A. E. 1977. Review of the Oligocene Cetacea. *Systematic Biology*, **25**, 304-320.

Wilson, L. E. 1935. Miocene marine mammals from the Bakersfield region, California. *Bulletin of the Peabody Museum of Natural History*, **4**, 1-143.

Zúñiga-Rivero F. J., Klein G. D., Hay-Roe H. & Álvarez-Calderon E. 2010. *The hydrocarbon potential of Peru.* BPZ Exploración & Producción S.R.L., Lima, Peru, 338 pp.

Appendix 1. List of silicoflagellate taxa from sample PN2.

Corbisema triacantha (Ehrenberg 1844) Hanna 1931

Distephanopsis crux subsp. *scutulata* (Bukry) Desikachary & Prema 1996

Naviculopsis obtusarca Bukry 1978 (DSDP44-37)

N. obtusarca Bukry var. *acicula* Bukry 1985

N. ponticula subsp. *ponticula* (Ehrenberg) Bukry 1982

Naviculopsis sp. 2 Cisielsky 1991

Table captions

Table 1. Measurements (in mm) of the skull of *Inticetus vertizi* MUSM 1980 (holotype). e estimate, + incomplete, - missing data.

Table 2. Measurements (in mm) and number of accessory denticles for the upper and lower teeth of *Inticetus vertizi* MUSM 1980 (holotype). e estimate, + incomplete, - missing data.

Table 3. Measurements (in mm) of the vertebrae of *Inticetus vertizi* MUSM 1980 (holotype). e estimate, + incomplete, ++ very incomplete, - missing data. Roman numbers for post-cervical vertebrae indicate that the identification is only tentative.

Figure captions

Figure 1. Map of the northern part of the Pisco Basin, southern coast of Peru, indicating several fossil-rich localities of the Pisco Formation (Cerro Colorado, Cerro los Quesos, and Cerro la Bruja) and Chilcatay Formation (Roca Negra, Ullujaya, and Zamaca). Roca Negra (black star) is the locality where *Inticetus vertizi* MUSM 1980 (holotype) was found. Modified from Lambert *et al.* (2014).
Planned for column width.

Figure 2. Stratigraphic column of part of the lower unit of the Chilcatay Formation in the Roca Negra locality, providing the relative position of *Inticetus vertizi* MUSM 1980 (holotype) and of the sample PN2 having yielded a biostratigraphically informative silicoflagellate assemblage (Early Miocene, late early Burdigalian).
Planned for column width.

Figure 3. Cranium and mandibles of *Inticetus vertizi* MUSM 1980 (holotype). **A,** dorsal view; **B,** corresponding explanatory line drawing; **C,** detail of the posterior part with a different lighting. Scale bars equal 200 mm.

Figure 4. Cranium and mandibles of *Inticetus vertizi* MUSM 1980 (holotype). **A,** left lateral view; **B,** corresponding explanatory line drawing. Scale bar equals 200 mm.

Figure 5. Cranium and mandibles of *Inticetus vertizi* MUSM 1980 (holotype). **A,** ventral view; **B,** corresponding explanatory line drawing. Scale bar equals 200 mm.

Figure 6. Cranium and mandibles of *Inticetus vertizi* MUSM 1980 (holotype). **A,** detail of the neurocranium region in left lateral view; **B,** corresponding explanatory line drawing. Scale bar equals 100 mm.

Figure 7. Cranium and mandibles of *Inticetus vertizi* MUSM 1980 (holotype). **A,** detail of the left side of the basicranium in ventrolateral view; **B,** corresponding explanatory line drawing. Grey areas for sediment; hatched areas for broken surfaces. Scale bar equals 100 mm.

Figure 8. Cranium of *Inticetus vertizi* MUSM 1980 (holotype) in posterior view. Scale bar equals 100 mm.

Figure 9. Right periotic of *Inticetus vertizi* MUSM 1980 (holotype). **A,** ventral view; **B,** corresponding explanatory line drawing; **C,** ventral view with accessory ossicle removed; **D,** medial view; **E,** dorsomedial and slightly anterior view; **F,** corresponding explanatory line drawing; **G,** dorsal view; **H,** lateral view. Abbreviations: crista interfen, crista interfenestralis; lateral ctp; lateral caudal tympanic process; medial ctp, medial caudal tympanic process. Grey areas for main openings; hatched areas for broken surfaces. Periotic whitened with ammonium chloride. Scale bar equals 30 mm.

Figure 10. Right tympanic bulla of *Inticetus vertizi* MUSM 1980 (holotype). **A,** medial view; **B,** corresponding explanatory line drawing; **C,** ventral view; **D,** dorsal view; **E,** lateral view; **F,** corresponding explanatory line drawing; **G,** posterior view; **H,** anterior view. Grey areas for sediment; hatched areas for broken surfaces. Tympanic whitened with ammonium chloride. Scale bar equals 30 mm.

Figure 11. Right malleus of *Inticetus vertizi* MUSM 1980 (holotype). **A,** explanatory line drawing in posteromedial view; **B,** corresponding photo; **C,** posteroventrolateral view. Scale bar equals 2 mm.

Figure 12. Detached upper teeth of *Inticetus vertizi* MUSM 1980 (holotype). **A-F,** right I^1 in labial (A), lingual (B), mesial (C), and distal (D) view, and detail of the crown in distolingual (E) and mesiolingual (F) view; **G-L,** right canine in labial (G), lingual (H), mesial (I), and distal (J) view, and detail of the crown in distolingual (K) and mesial (L) view. Scale bar equals 10 mm.

Figure 13. Cranium and mandibles of *Inticetus vertizi* MUSM 1980 (holotype). Detail of the anterior part of the rostrum and mandible in oblique right anterolateral and slightly dorsal view, showing upper and lower anterior teeth. For the size of elements, refer to more orthogonal views.
Planned for column width.

Figure 14. Cranium and mandibles of *Inticetus vertizi* MUSM 1980 (holotype). **A,** detail of the anterior part of the rostrum and mandible in right lateral view; **B,** corresponding explanatory line drawing; **C-E,** enlarged views of anterior cheek teeth and incisors. Scale bar for A-B equals 100 mm.

Figure 15. Cranium and mandibles of *Inticetus vertizi* MUSM 1980 (holotype). **A,** detail of the anterior part of the rostrum and mandible in left lateral view; **B-E,** enlarged views of incisors, upper canine, and anterior cheek teeth C_2 and C^5; F, detail of the accessory denticles on the distal carina of C^5. Scale bar for A equals 100 mm.

Figure 16. Cranium and mandibles of *Inticetus vertizi* MUSM 1980 (holotype). **A,** detail of the posterior part of the rostrum and mandible in right lateral view, with anterior part of the rostrum removed; **B-D,** detail of cheek teeth C^9, C^8, C^7, and C_6. Scale bar for A equals 50 mm.

Figure 17. Cranium and mandibles of *Inticetus vertizi* MUSM 1980 (holotype). **A,** detail of the posterior part of the right lower quadrant including cheek teeth $C_{8\text{-}12}$, in medial view; **B,** corresponding explanatory line drawing. Scale bar equals 50 mm.

Figure 18. Fragment of the atlas of *Inticetus vertizi* MUSM 1980 (holotype). **A,** anterior view; **B,** posterior view. Scale bar equals 20 mm.

Figure 19. Axis and cervicals C3-C7 of *Inticetus vertizi* MUSM 1980 (holotype). **A-D,** axis and C3-C5 in anterior view (A), corresponding explanatory line drawing (B), right anterodorsolateral (C), and ventral (D) view; **E-F,** C6-C7 in anterior (E) and ventral (F) view. Scale bar equals 20 mm.

Figure 20. Thoracic vertebrae of *Inticetus vertizi* MUSM 1980 (holotype). **A-B,** ThI in posterior (A) and dorsal (B) view; **C-D,** ThII in anterior (C) and left lateral (D) view; **E,** ThIII in anterior/posterior view; **F,** ThIV in right lateral view; **G,** ThIV-VI in a single block with a rib fragments; **H-J,** ThVII in posterior (H), right lateral (I), and dorsal (J) view; **K,** ThIX in right lateral view; **L-M,** ThXI in anterior/posterior (L) and lateral (M) view. Scale bar equals 20 mm.

Figure 21. Lumbar vertebrae of *Inticetus vertizi* MUSM 1980 (holotype). **A,** LuIII in ventral view; **B,** LuVI in dorsal view; **C,** LuVII in ventral view; **D-E,** LuVIII in ventral (D) and anterior/posterior (E) view; **F,** LuIX in ventral view. Scale bar equals 20 mm.
Planned for column width.

Figure 22. Caudal vertebrae of *Inticetus vertizi* MUSM 1980 (holotype). **A,** CaI in ventral view; **B,** CaII in ventral view; **C,** CaIII in ventral view; **D,** CaVI in ?right lateral view; **E,** CaVII in ?left lateral view; **F,** CaVIII in ?left lateral view; **G,** CaIX in lateral view; **H,** CaX in lateral view; **I-J,** CaXI in anterior/posterior (I) and lateral (J) view; **K-M,** CaXII in anterior/posterior (K), lateral (L), and ventral (M) view; **N-O,** CaXIII in anterior/posterior (N) and ?ventral (O) view; **P-Q,** CaXIV in anterior/posterior (P) and ?ventral (Q) view; **R-S,** CaXV in anterior/posterior (R) and ?ventral (S) view; **T,** CaXVI in anterior view; **U-V,** CaXVI + CaXVII in left lateral (U) and ventral (V) view. Scale bar equals 20 mm.

Figure 23. Chart showing changes in the dimensions (in mm) of vertebral central (namely length, height and width) along the vertebral column of *Inticetus vertizi* MUSM 1980 (holotype). Numbers on the horizontal axis correspond to a sequence from cervical C3 on the left to the last preserved caudals on the right, as listed in Table 3. Some vertebrae could be missing and several centra were too incomplete to be measured for one or more of their dimensions.

Figure 24. Sternum of *Inticetus vertizi* MUSM 1980 (holotype). **A-B,** manubrium in dorsal (A), ventral (B), and right lateral (C) view; **D-F,** second sternebra in ?dorsal (D), ?ventral (E), and anterior (F) view. Scale bar equals 20 mm.

Figure 25. Ribs of *Inticetus vertizi* MUSM 1980 (holotype). The rib fragments are organized in an anteroposterior sequence from the lower part of the figure to the top, except for the two lower distal fragments. Scale bar equals 50 mm.

Figure 26. Strict consensus tree for the phylogenetic analysis with equally weighted characters and without molecular constraint (analysis 1), resulting in the placement of *Inticetus vertizi* as a stem Odontoceti.

Figure 27. Alternative relationships of *Inticetus vertizi* resulting from other phylogenetic analyses. **A,** strict consensus tree for the analysis with down-weighted homoplastic characters and without molecular constraint (analysis 2), placing *I. vertizi* in a large Platanistoidea clade; **B,** strict consensus tree for the analysis with equally weighted homoplastic characters and with molecular constraint (analysis 3), placing *I. vertizi* as a stem Odontoceti; **C,** strict consensus tree for the analysis with down-weighted homoplastic characters and with molecular constraint (analysis 4), placing *I. vertizi* in a large Platanistoidea clade.

Figure 28. Schematic drawing showing the position of the partly articulated skeleton of *Inticetus vertizi* MUSM 1980 (holotype) as found in the field, together with three shark teeth (black triangles). Detail photograph and interpretive drawing of the rostrum and mandible of MUSM 1980 in left lateral view, with shallow shark bite marks indicated. Scale bar for the skeleton equals 500 mm, scale bar for detail of the rostrum and mandible equals 50 mm, and scale bars for shark teeth equal 10 mm.

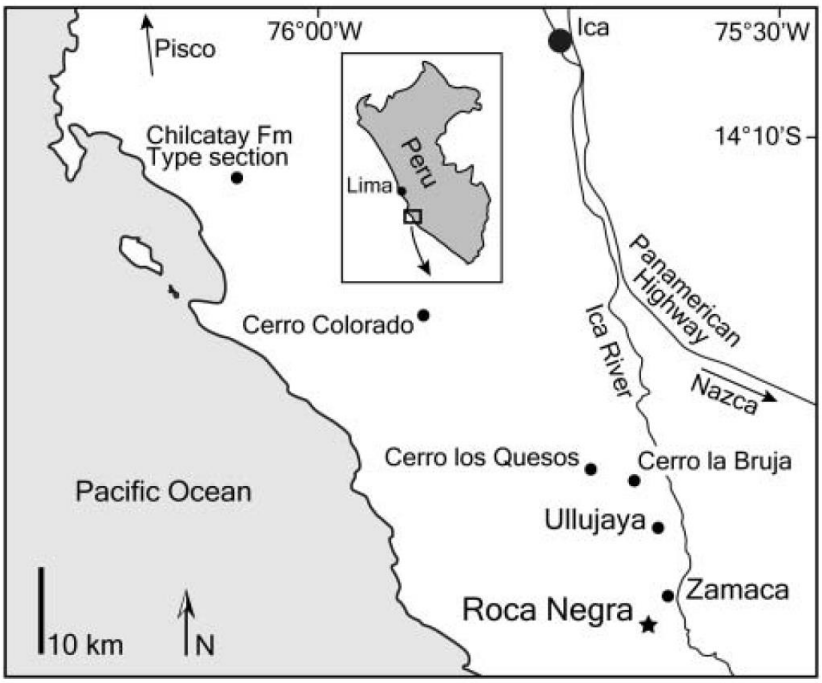
Pisco
76°00'W
Ica
75°30'W
14°10'S
Chilcatay Fm
Type section
Peru
Lima
Panamerican
Highway
Cerro Colorado
Ica River
Nazca
Cerro los Quesos
Cerro la Bruja
Pacific Ocean
Ullujaya
Zamaca
Roca Negra
10 km
N

Figure 1

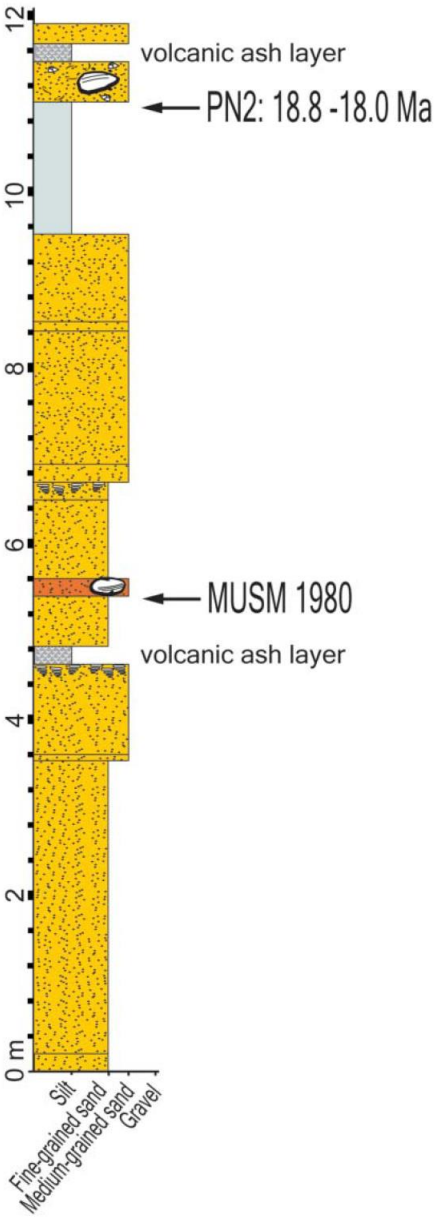
12
10
8
6
4
2
0 m
volcanic ash layer
PN2: 18.8 -18.0 Ma
MUSM 1980
volcanic ash layer
Silt
Fine-grained sand
Medium-grained sand
Gravel

Figure 2

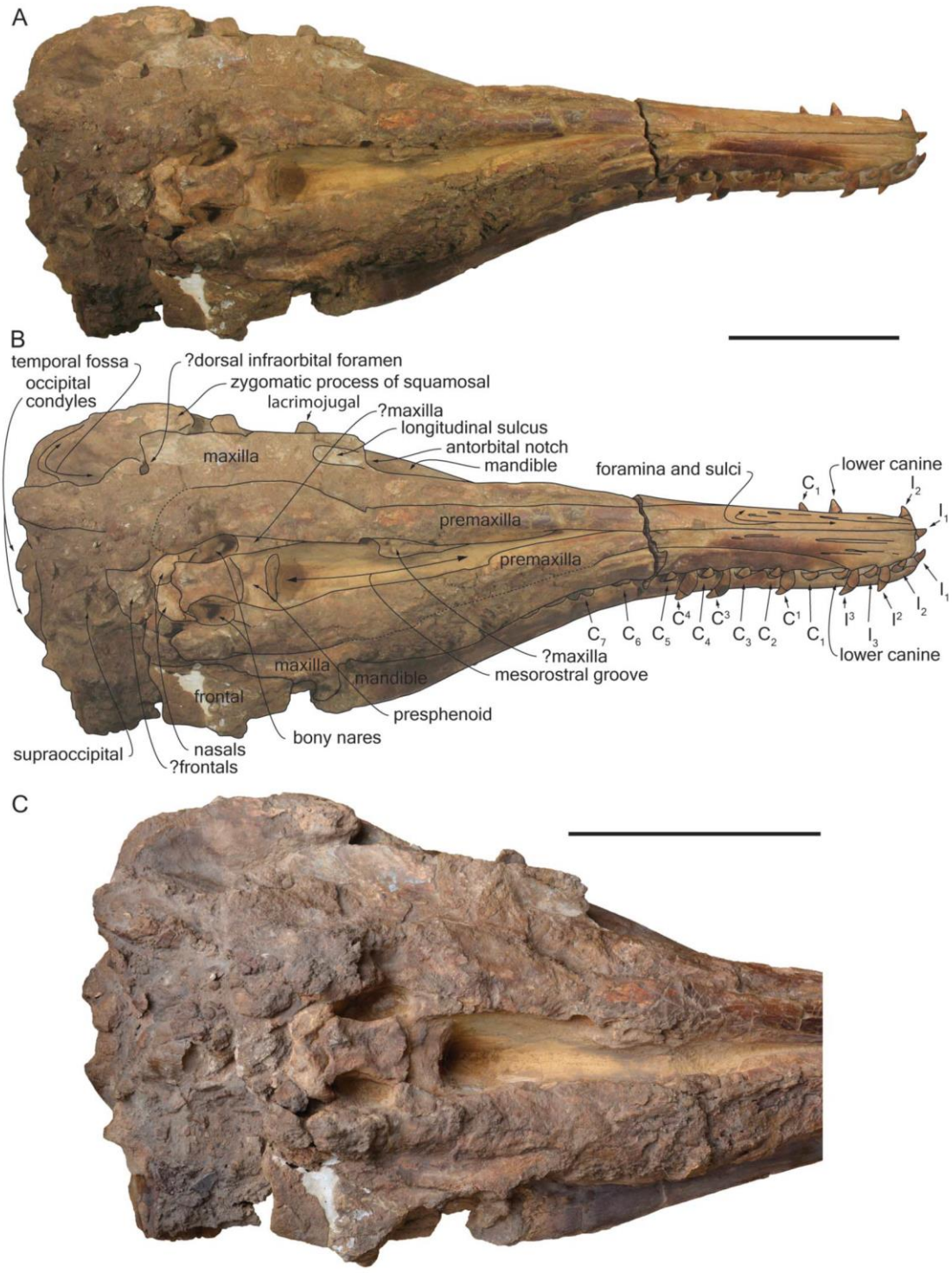
A
B
temporal fossa
occipital condyles
?dorsal infraorbital foramen
zygomatic process of squamosal
lacrimojugal
?maxilla
longitudinal sulcus
antorbital notch
mandible
maxilla
foramina and sulci
lower canine
premaxilla
premaxilla
maxilla
mandible
frontal
?maxilla
mesorostral groove
presphenoid
bony nares
supraoccipital
nasals
?frontals
lower canine
C
Figure 3

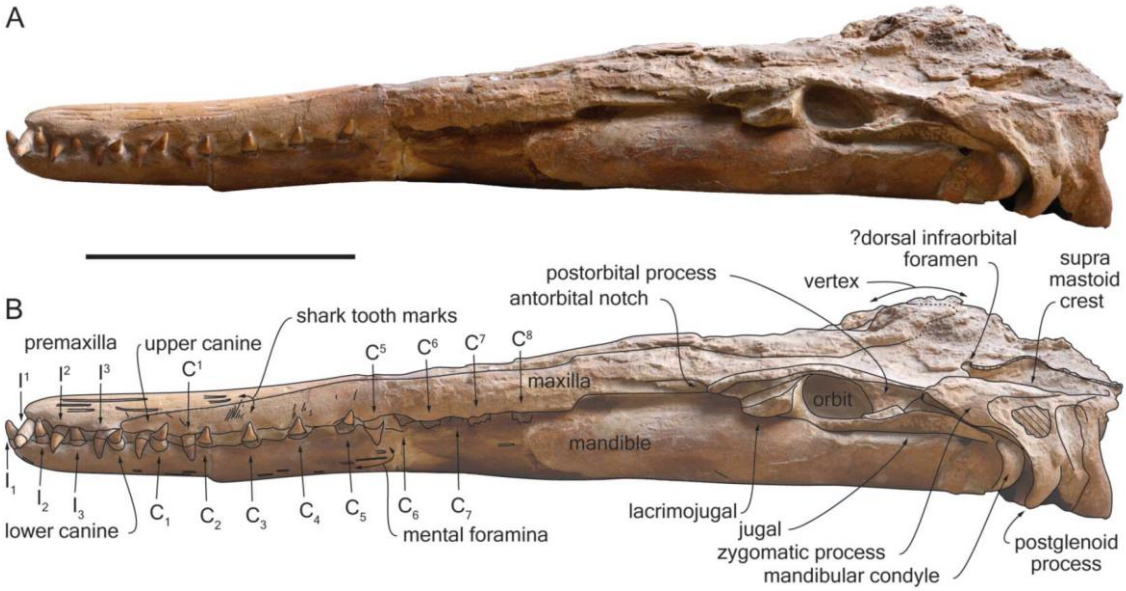
A
B
premaxilla
upper canine
shark tooth marks
I1
I2
I3
C1
C5
C6
C7
C8
maxilla
mandible
orbit
postorbital process
antorbital notch
?dorsal infraorbital foramen
vertex
supra mastoid crest
lacrimojugal
jugal
zygomatic process
mandibular condyle
postglenoid process
I1
I2
I3
C1
C2
C3
C4
C5
C6
C7
lower canine
mental foramina

Figure 4

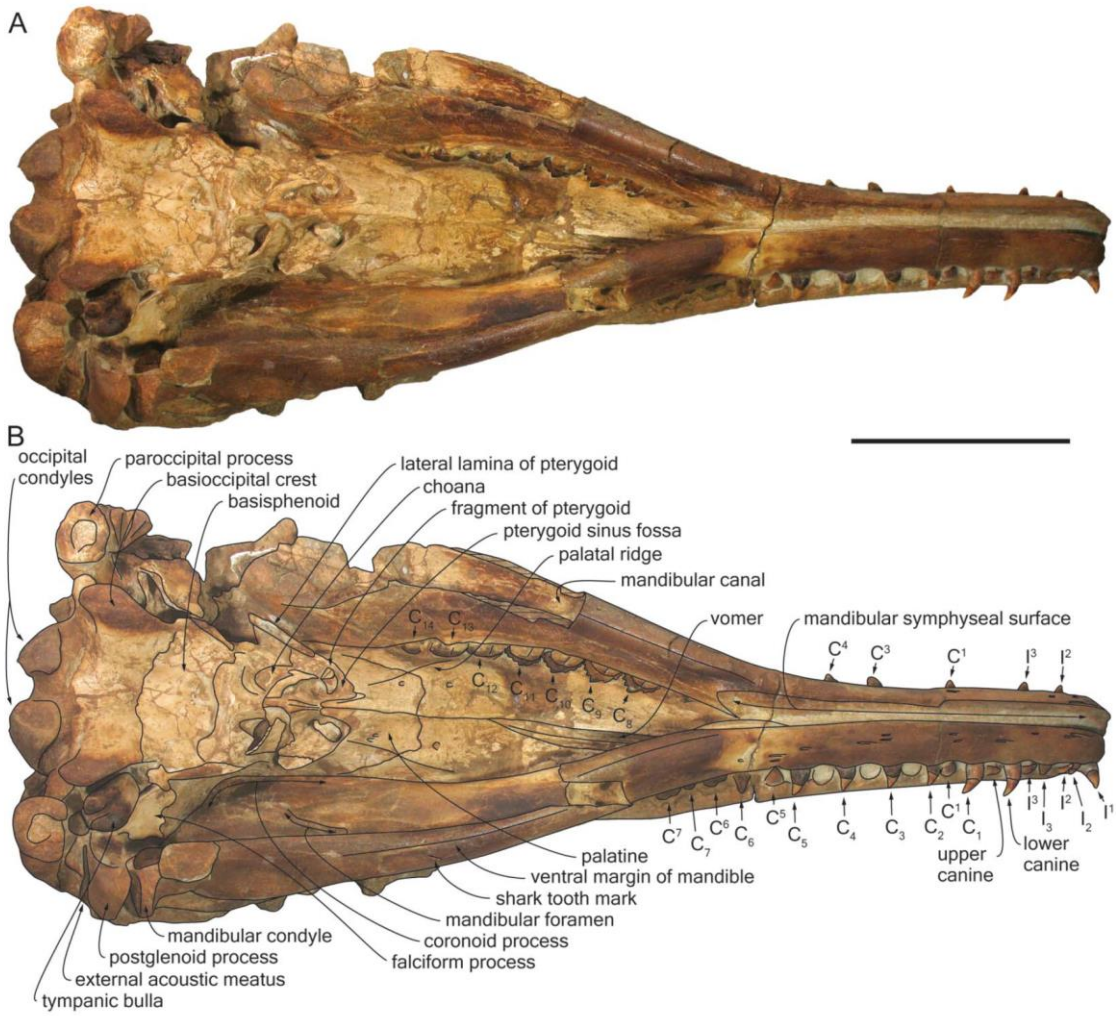
A
B
occipital condyles
paroccipital process
basioccipital crest
basisphenoid
lateral lamina of pterygoid
choana
fragment of pterygoid
pterygoid sinus fossa
palatal ridge
mandibular canal
vomer
mandibular symphyseal surface
palatine
ventral margin of mandible
shark tooth mark
mandibular foramen
coronoid process
falciform process
mandibular condyle
postglenoid process
external acoustic meatus
tympanic bulla
upper canine
lower canine

Figure 5

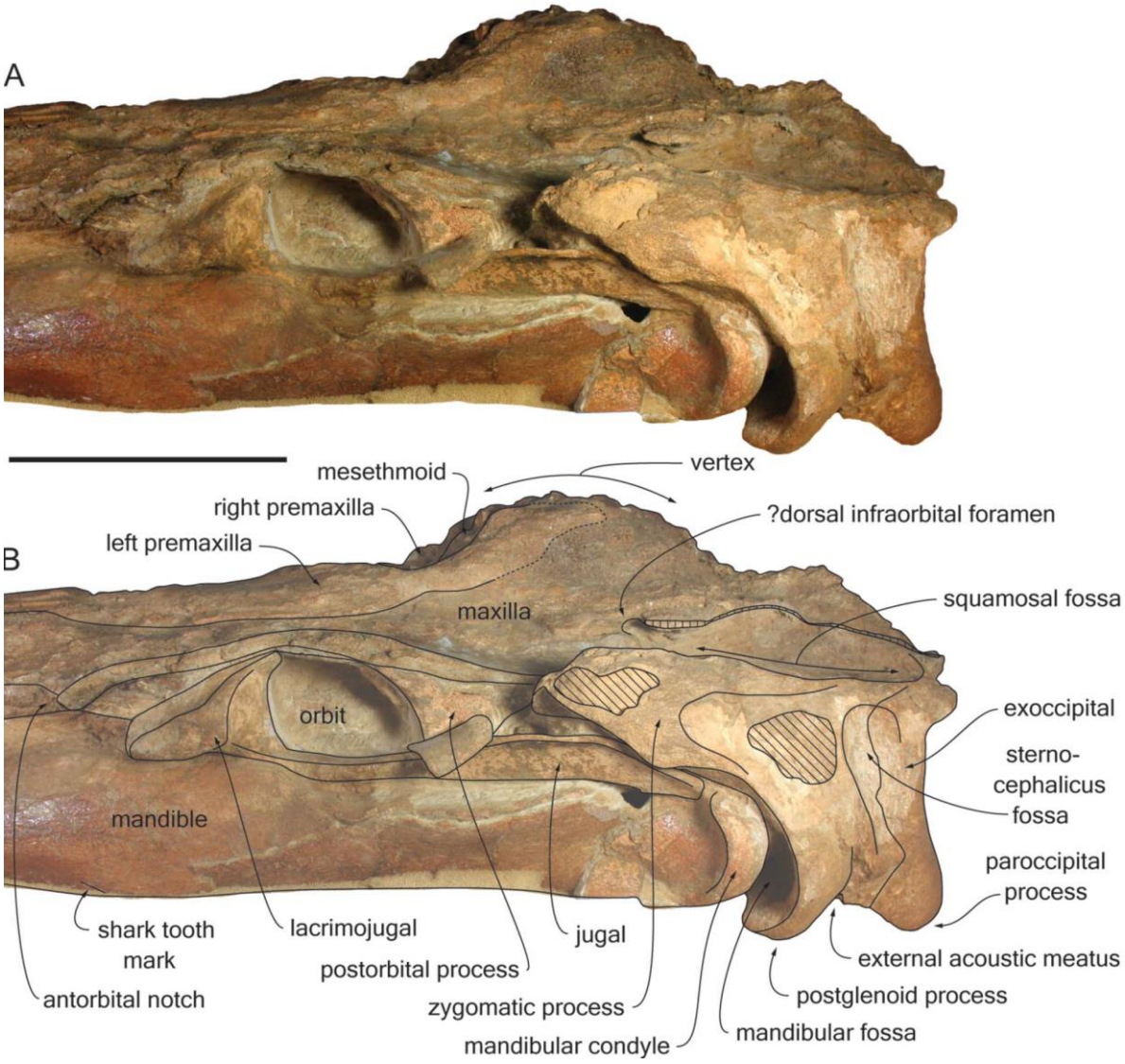
A
B
mesethmoid
vertex
right premaxilla
?dorsal infraorbital foramen
left premaxilla
maxilla
squamosal fossa
orbit
exoccipital
sterno-
cephalicus
fossa
mandible
paroccipital
process
shark tooth
mark
lacrimojugal
jugal
external acoustic meatus
postorbital process
antorbital notch
zygomatic process
postglenoid process
mandibular fossa
mandibular condyle

Figure 6

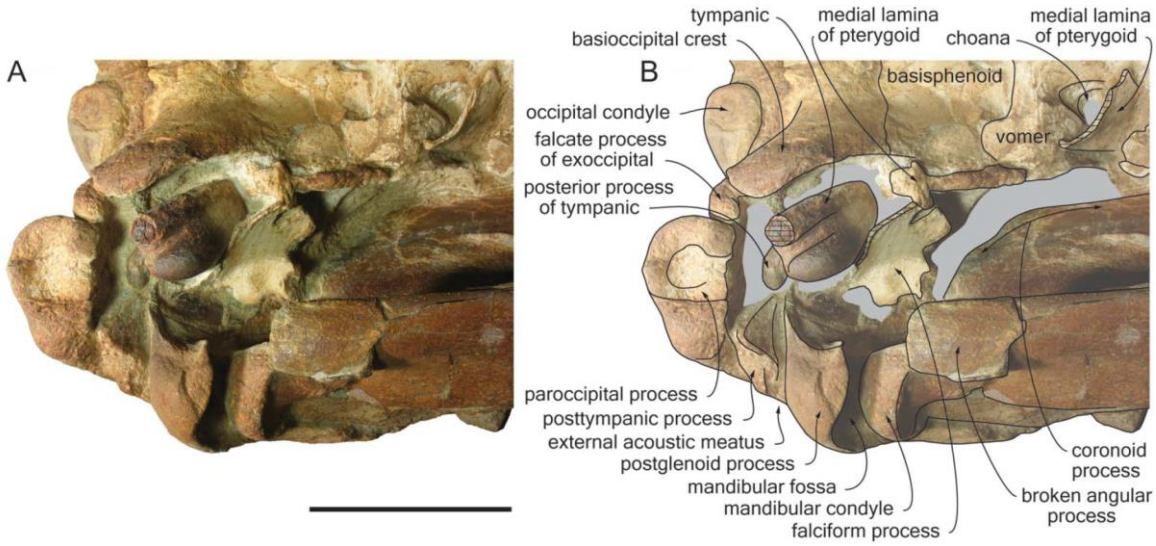
A
B
tympanic
basioccipital crest
medial lamina
of pterygoid
choana
medial lamina
of pterygoid
basisphenoid
occipital condyle
falcate process
of exoccipital
posterior process
of tympanic
vomer
paroccipital process
posttympanic process
external acoustic meatus
postglenoid process
mandibular fossa
mandibular condyle
falciform process
coronoid
process
broken angular
process

Figure 7

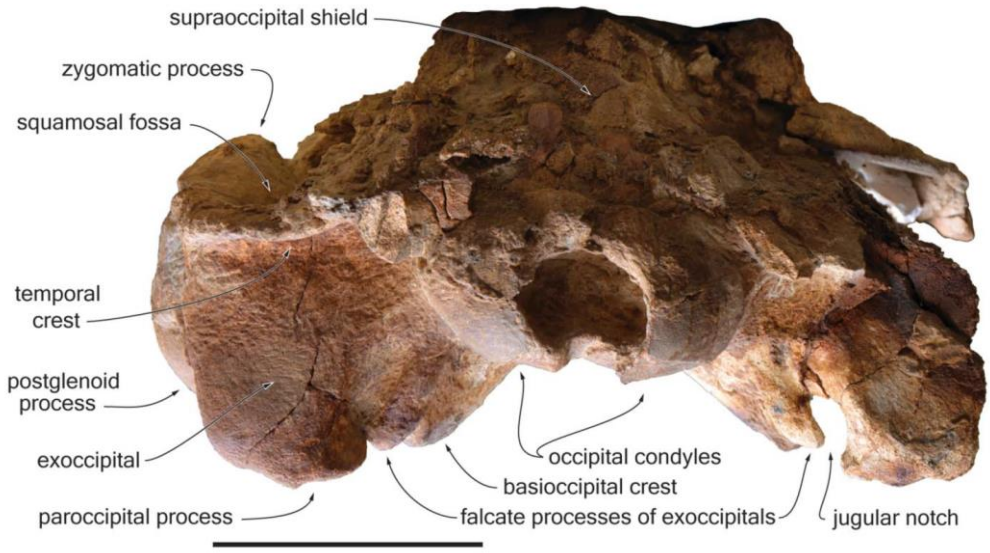
supraoccipital shield
zygomatic process
squamosal fossa
temporal crest
postglenoid process
exoccipital
paroccipital process
occipital condyles
basioccipital crest
falcate processes of exoccipitals
jugular notch

Figure 8

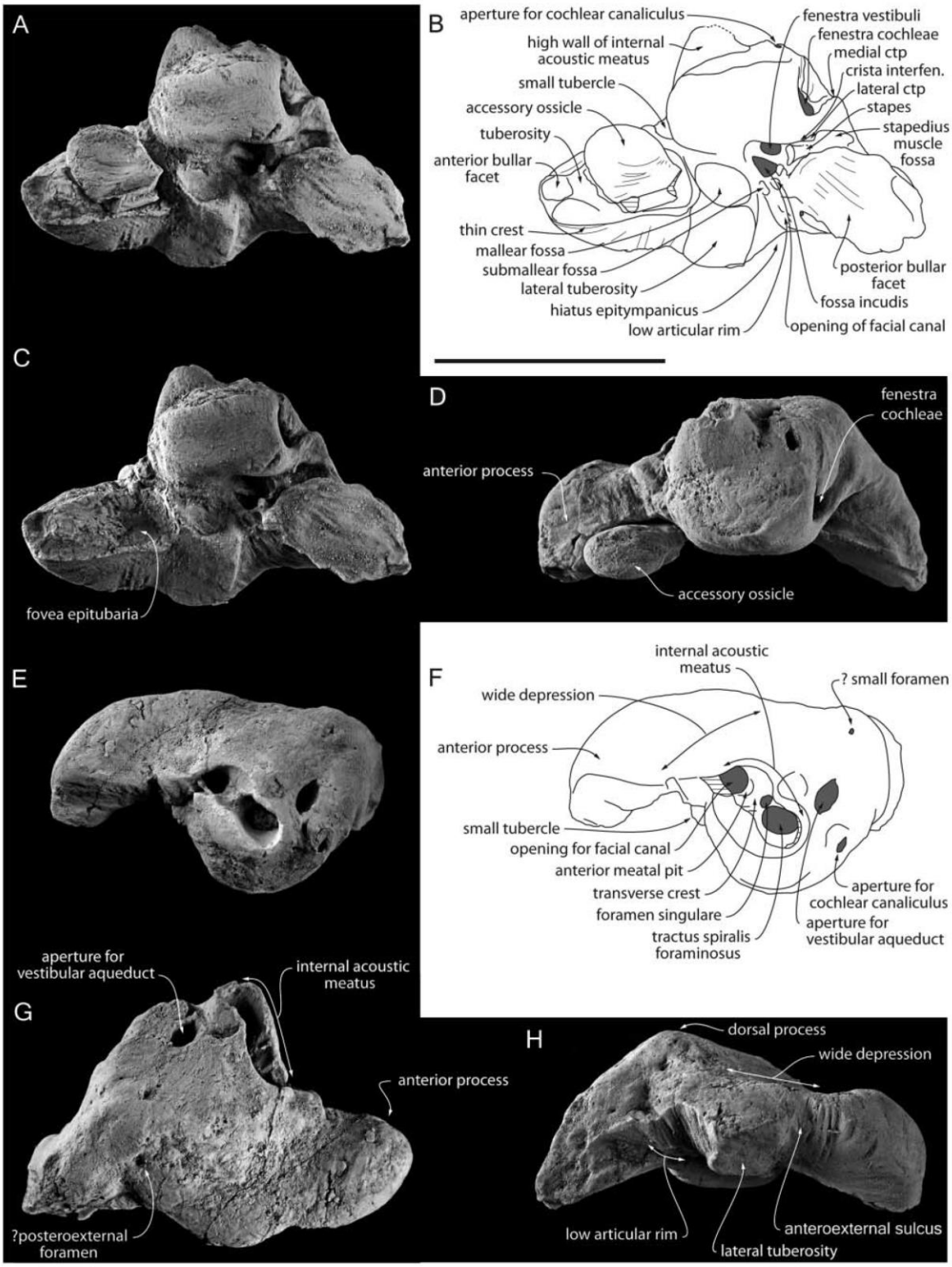
A
B
aperture for cochlear canaliculus
high wall of internal acoustic meatus
small tubercle
accessory ossicle
tuberosity
anterior bullar facet
thin crest
mallear fossa
submallear fossa
lateral tuberosity
hiatus epitympanicus
low articular rim
fenestra vestibuli
fenestra cochleae
medial ctp
crista interfen.
lateral ctp
stapes
stapedius muscle fossa
posterior bullar facet
fossa incudis
opening of facial canal
C
fovea epitubaria
D
fenestra cochleae
anterior process
accessory ossicle
E
F
internal acoustic meatus
? small foramen
wide depression
anterior process
small tubercle
opening for facial canal
anterior meatal pit
transverse crest
foramen singulare
tractus spiralis foraminosus
aperture for cochlear canaliculus
aperture for vestibular aqueduct
G
aperture for vestibular aqueduct
internal acoustic meatus
anterior process
?posteroexternal foramen
H
dorsal process
wide depression
low articular rim
lateral tuberosity
anteroexternal sulcus

Figure 9

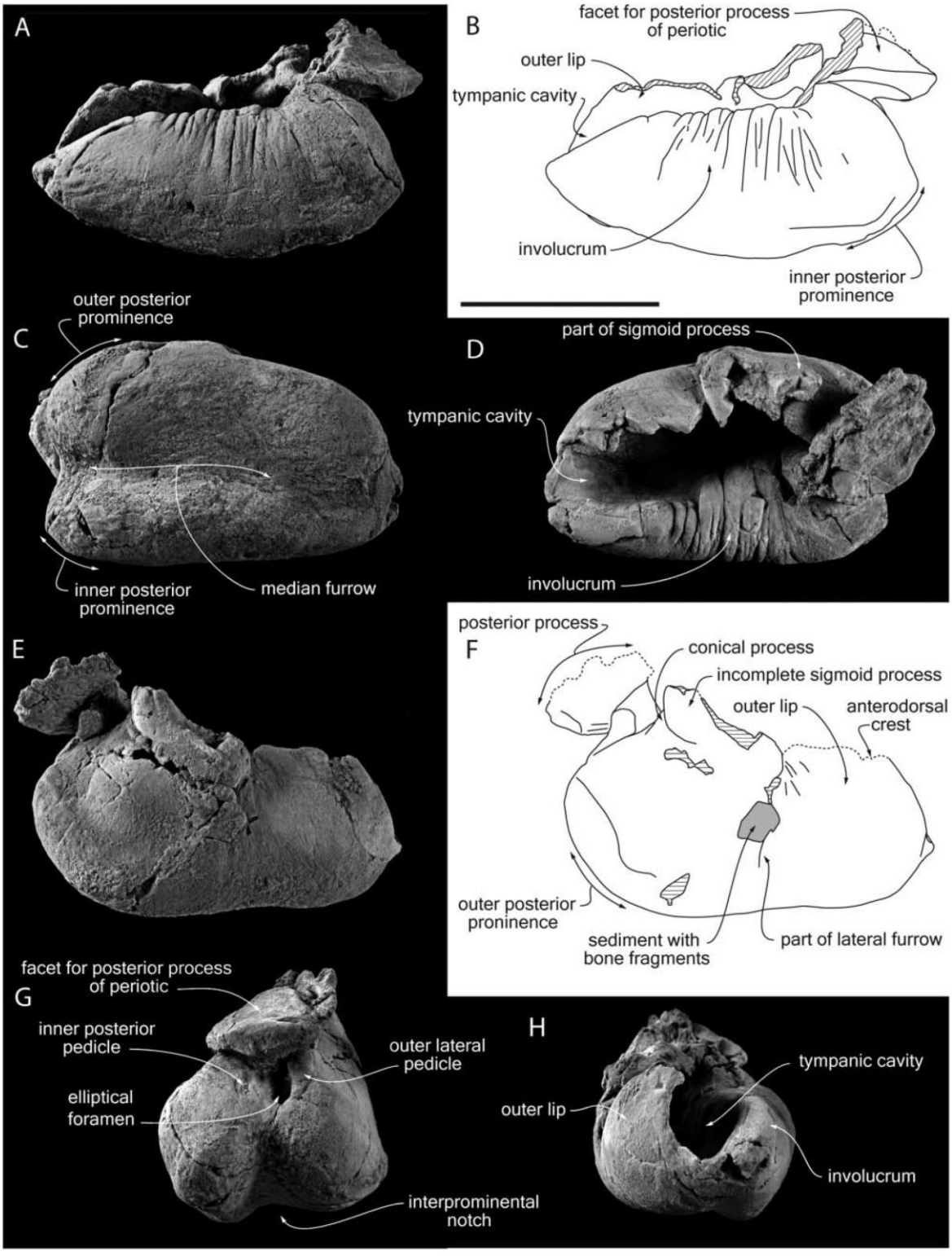
A
B
facet for posterior process of periotic
outer lip
tympanic cavity
involucrum
inner posterior prominence
outer posterior prominence
C
inner posterior prominence
median furrow
D
part of sigmoid process
tympanic cavity
involucrum
E
posterior process
F
conical process
incomplete sigmoid process
outer lip
anterodorsal crest
outer posterior proninence
sediment with bone fragments
part of lateral furrow
facet for posterior process of periotic
G
inner posterior pedicle
outer lateral pedicle
elliptical foramen
interprominental notch
H
tympanic cavity
outer lip
involucrum

Figure 10

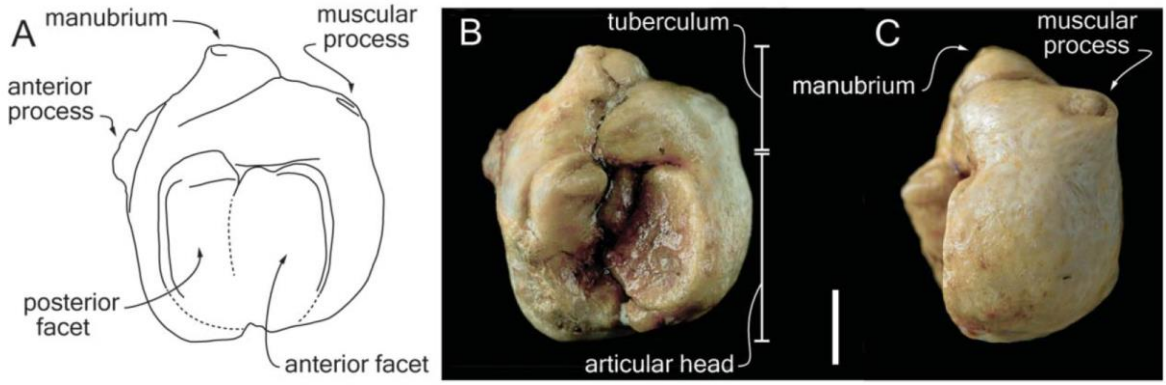
A
manubrium
muscular process
anterior process
posterior facet
anterior facet
B
tuberculum
articular head
C
manubrium
muscular process

Figure 11

Figure 12

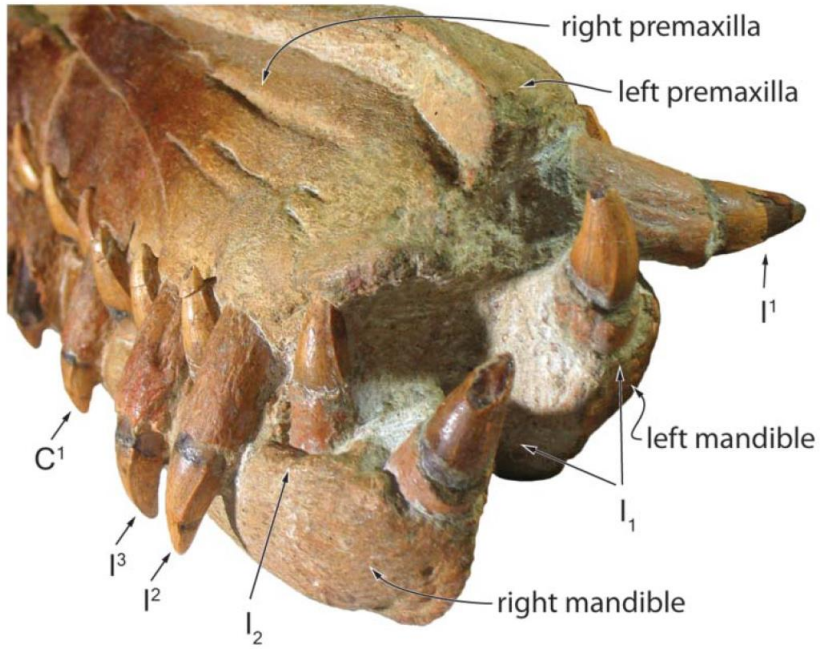
right premaxilla
left premaxilla
I1
left mandible
C1
I1
I3
I2
I2
right mandible

Figure 13

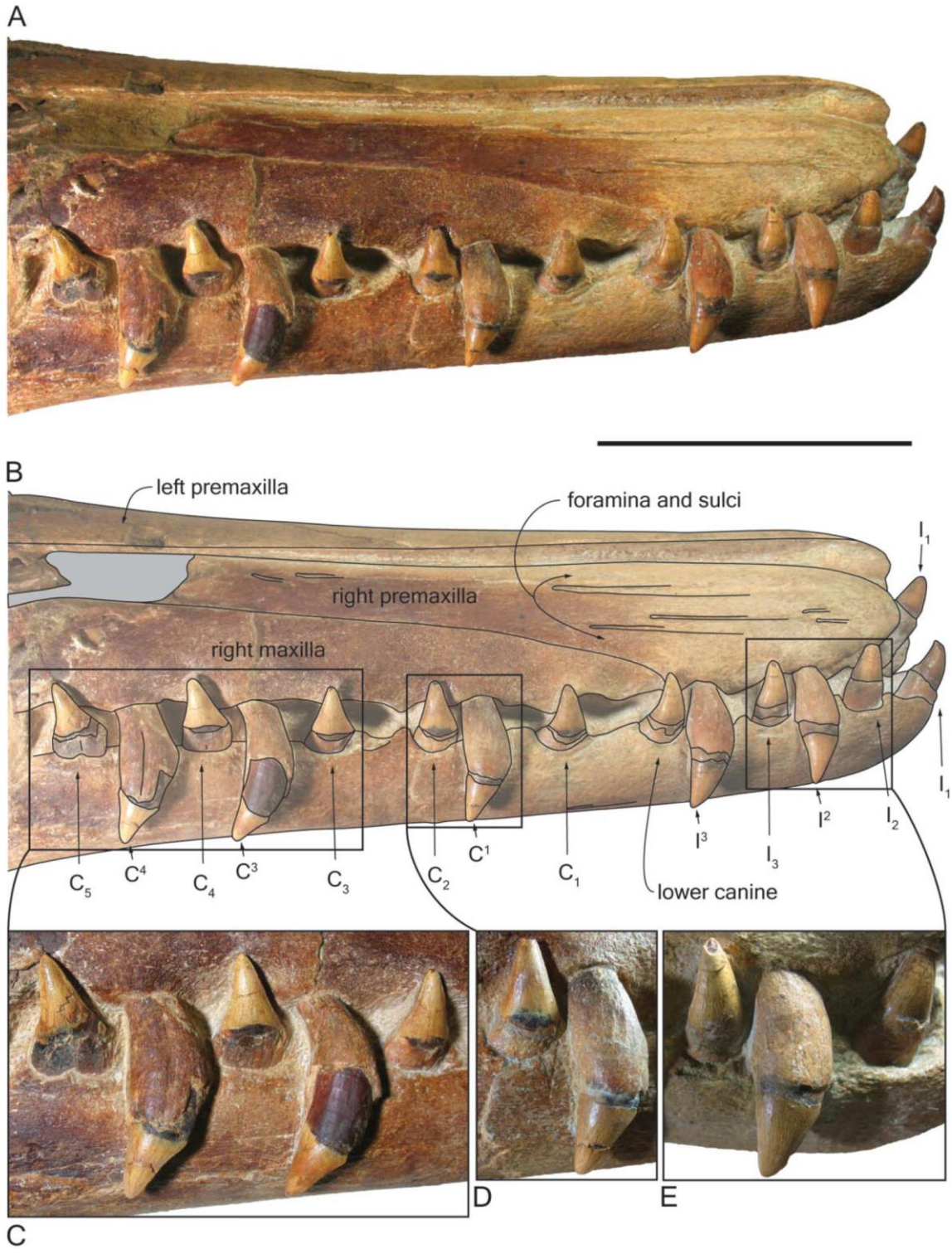
A
B
left premaxilla
foramina and sulci
right premaxilla
right maxilla
I1
I1
C5
C4
C4
C3
C3
C2
C1
C1
I3
I3
I2
I2
lower canine
C
D
E

Figure 14

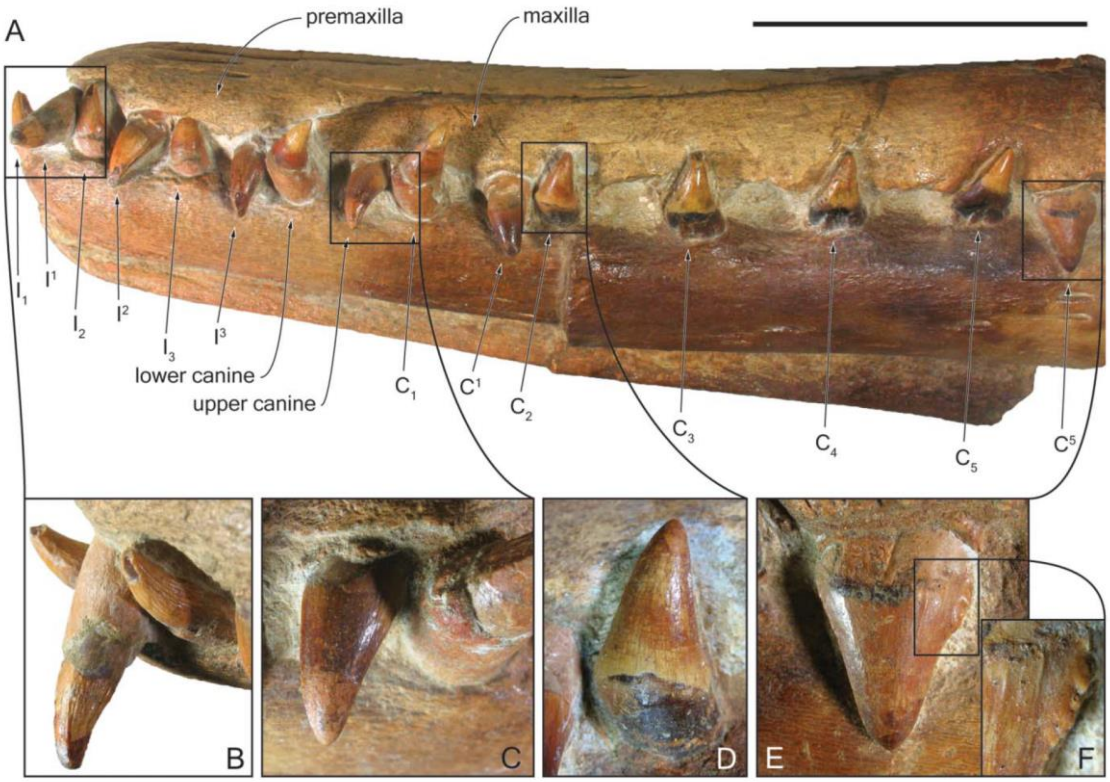
A
premaxilla
maxilla
I1
I1
I2
I2
I3
I3
lower canine
upper canine
C1
C1
C2
C3
C4
C5
C5
B
C
D
E
F

Figure 15

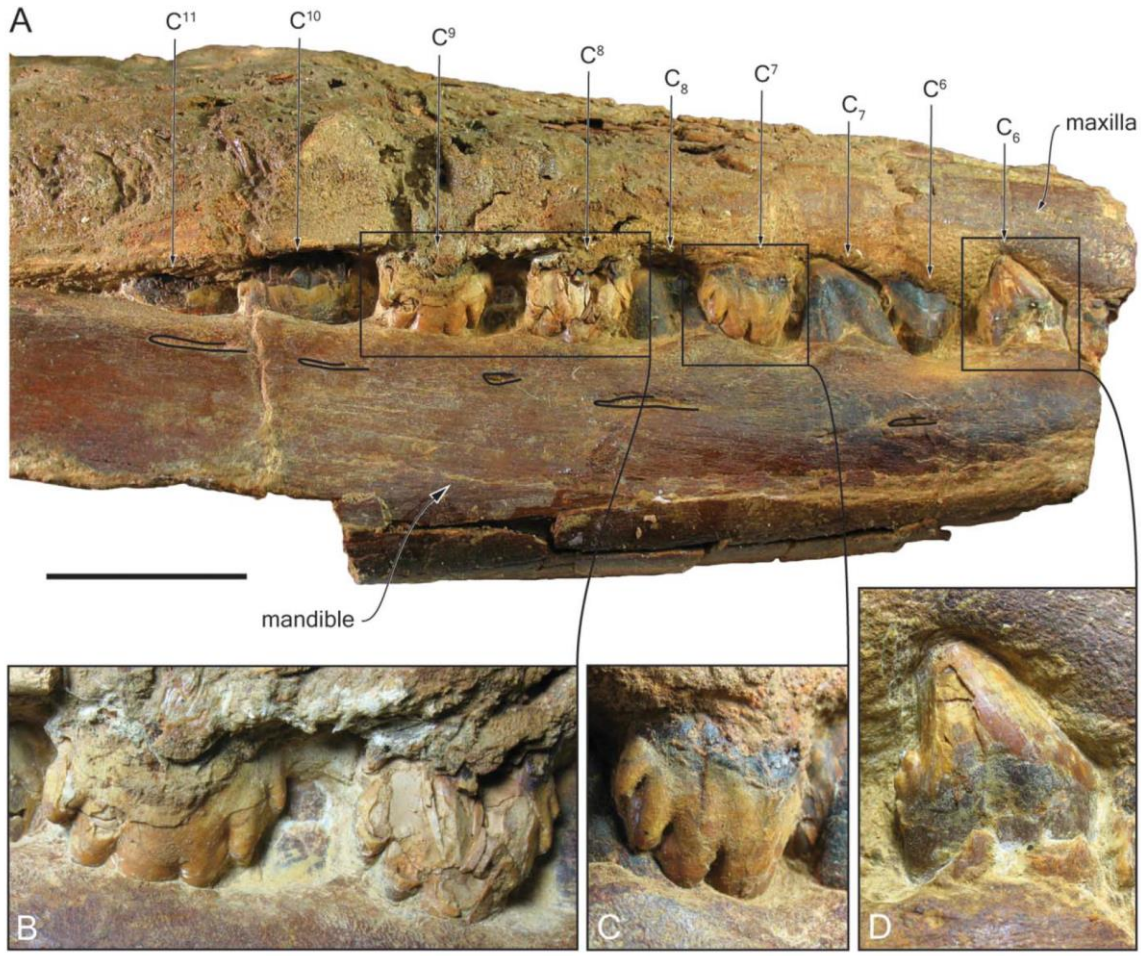

Figure 16

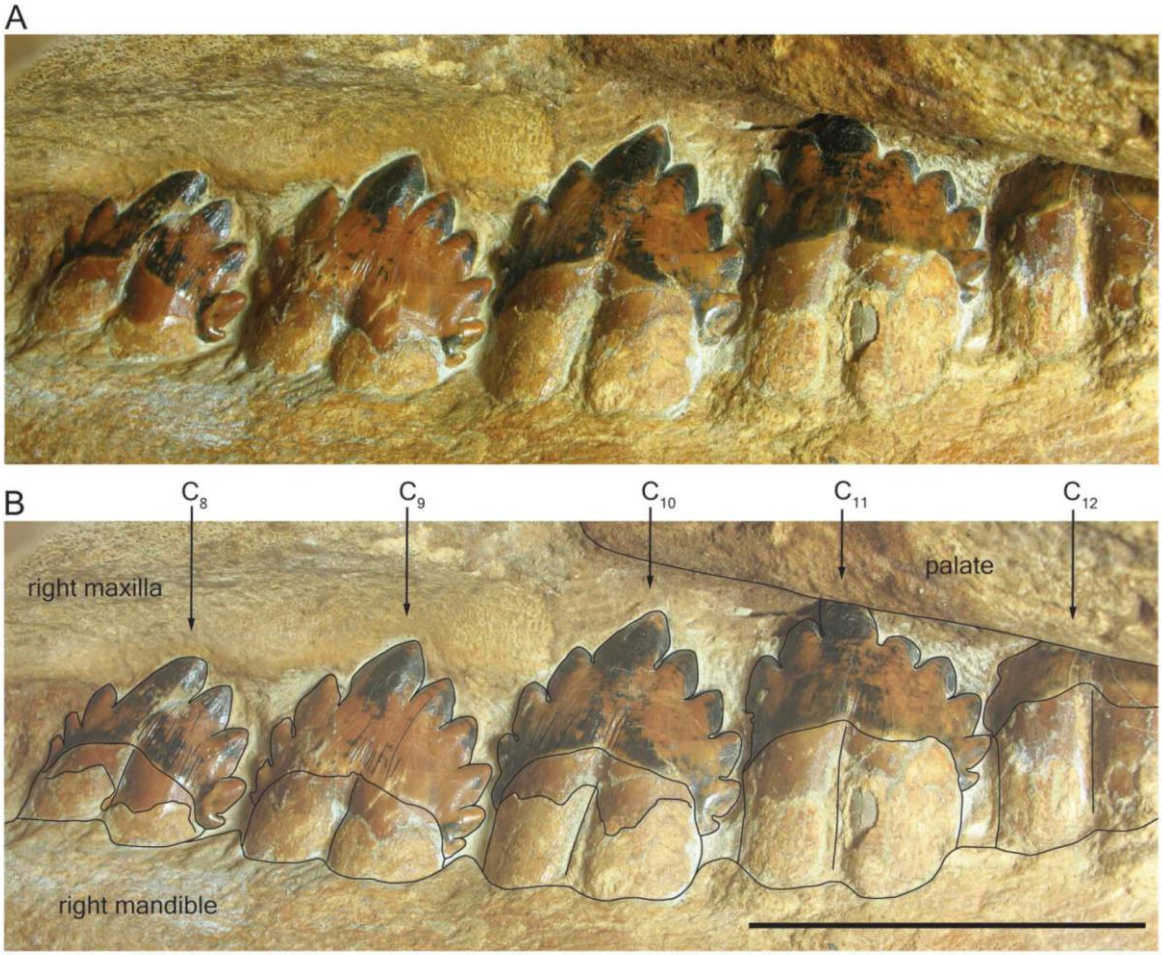

Figure 17

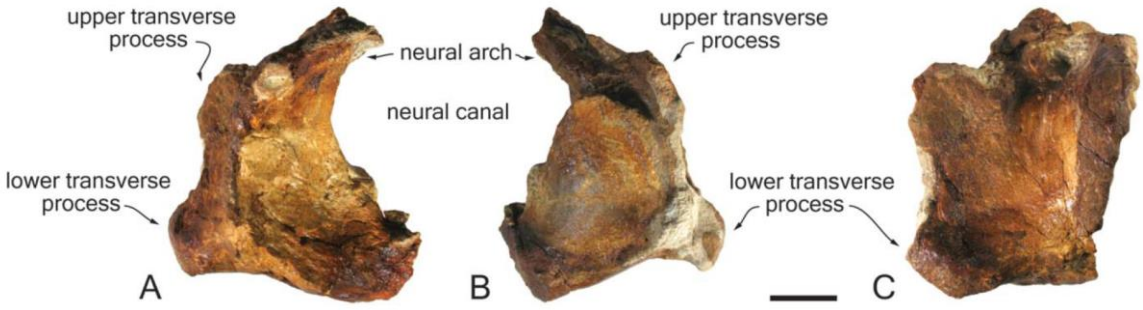
upper transverse process
neural arch
neural canal
lower transverse process
A
upper transverse process
lower transverse process
B
C

Figure 18

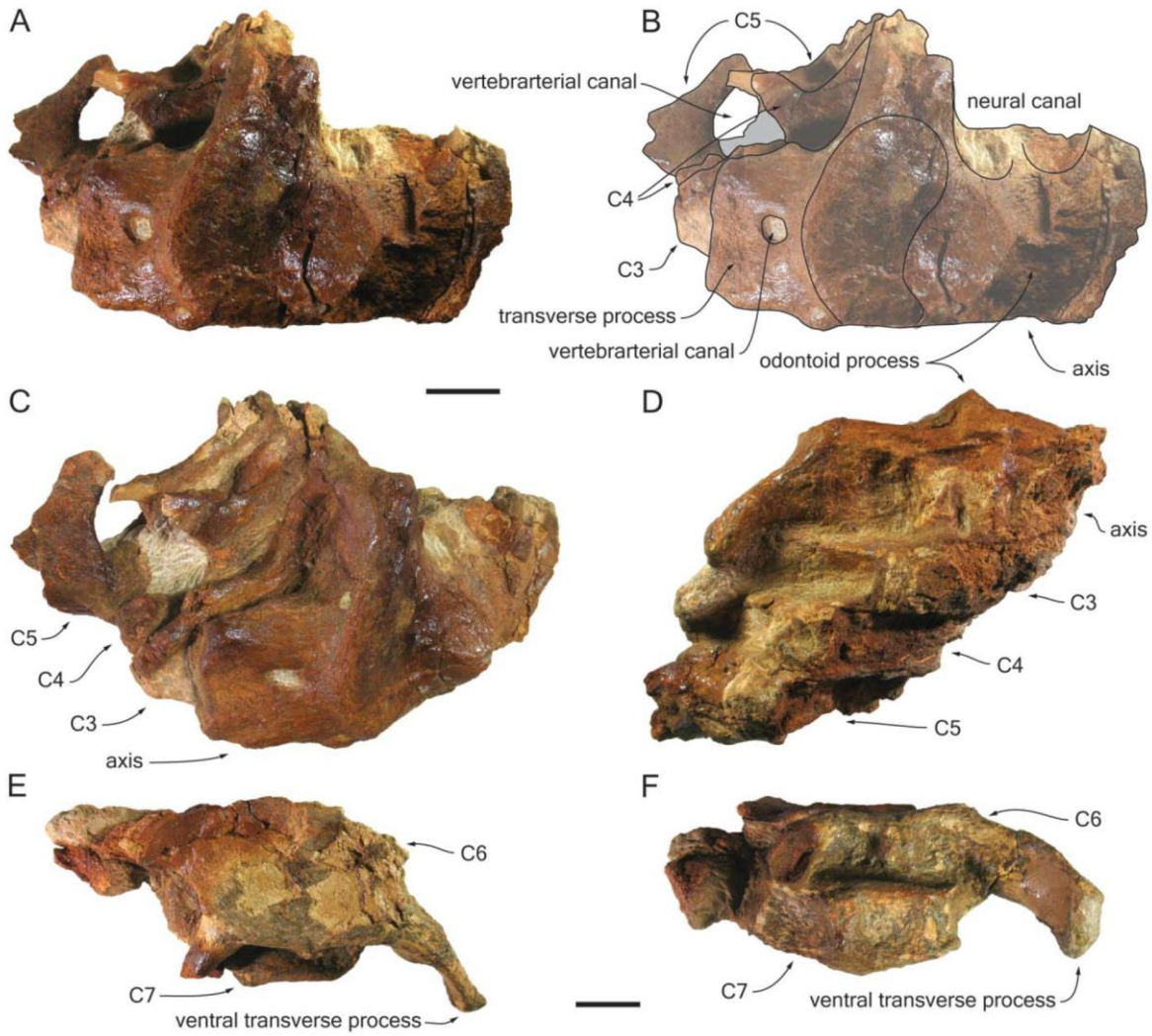
A
B
C5
vertebrarterial canal
neural canal
C4
C3
transverse process
vertebrarterial canal
odontoid process
axis
C
D
C5
C4
C3
axis
axis
C3
C4
C5
E
F
C6
C7
ventral transverse process
C6
C7
ventral transverse process

Figure 19

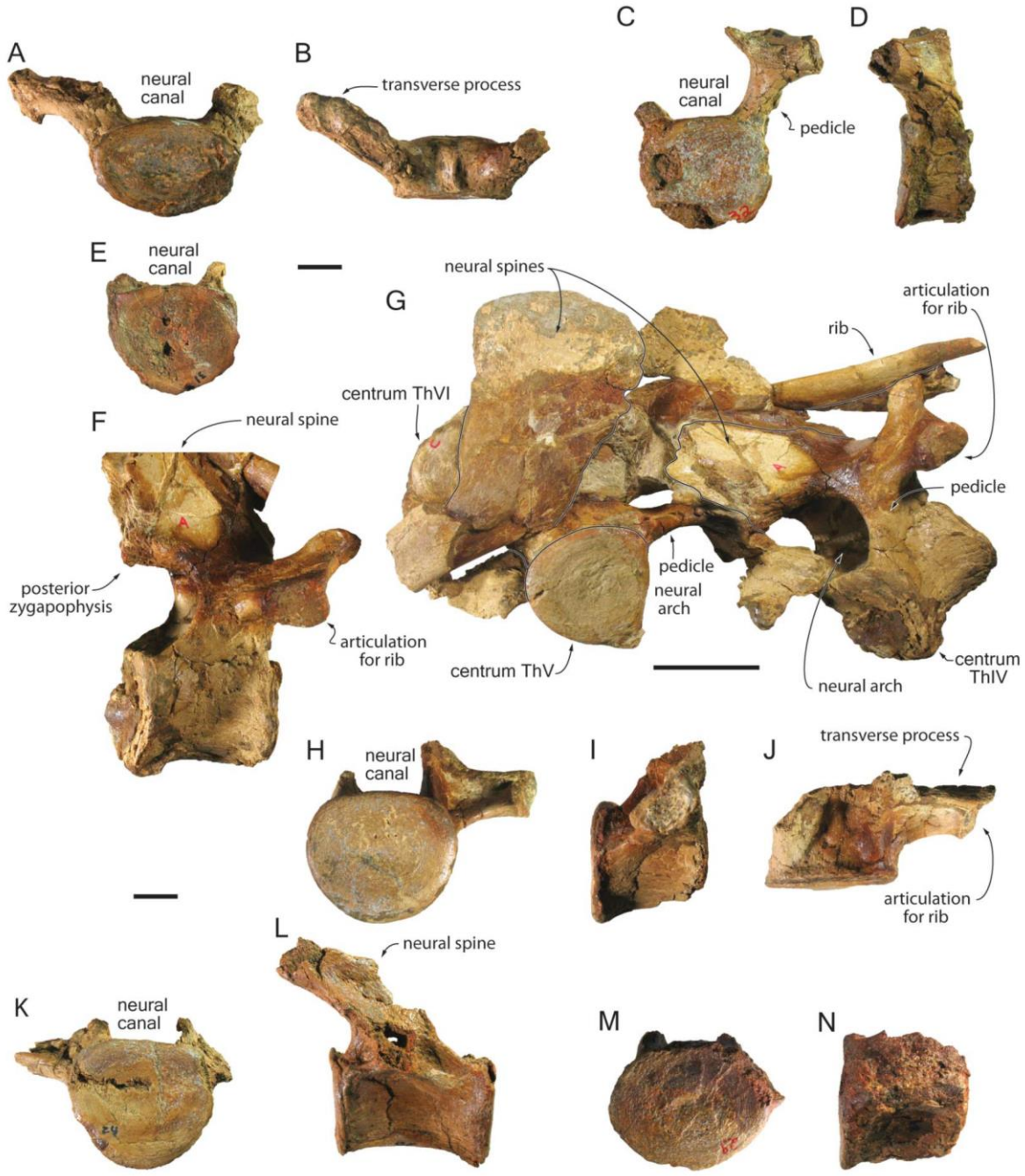
A
neural canal
B
transverse process
C
neural canal
pedicle
D
E
neural canal
F
neural spine
posterior zygapophysis
articulation for rib
G
neural spines
articulation for rib
rib
centrum ThVI
pedicle
pedicle
neural arch
centrum ThV
neural arch
centrum ThIV
H
neural canal
I
J
transverse process
articulation for rib
K
neural canal
L
neural spine
M
N

Figure 20

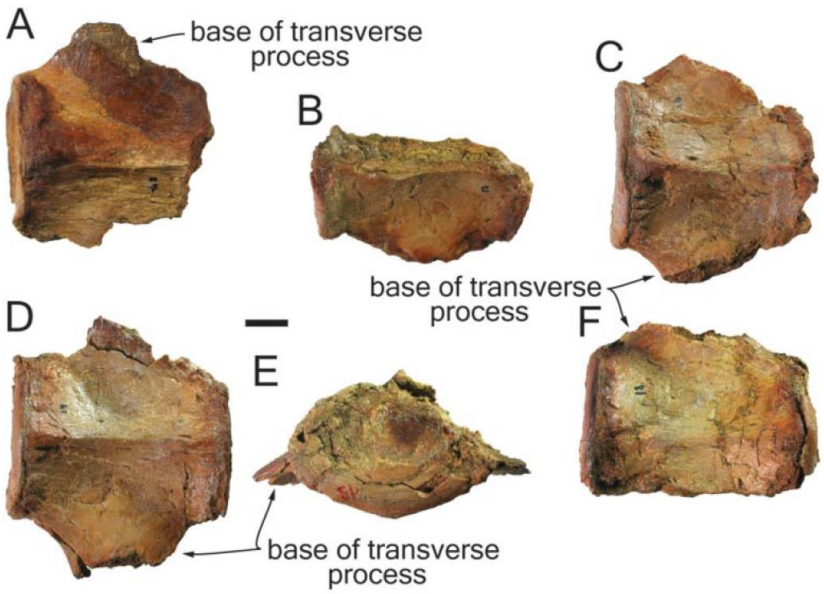
A
base of transverse process
B
C
base of transverse process
D
E
F
base of transverse process

Figure 21

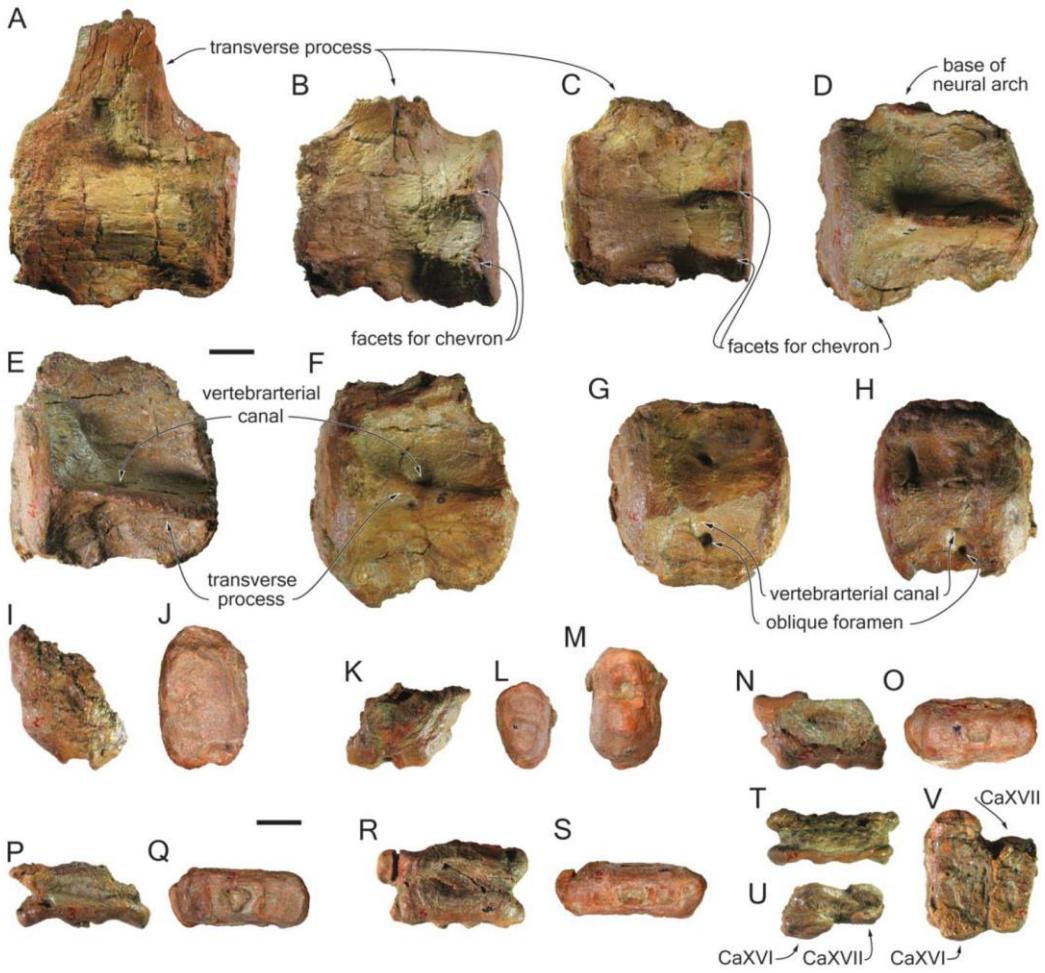
A
transverse process
B
C
D
base of
neural arch
facets for chevron
facets for chevron
E
F
vertebrarterial
canal
transverse
process
G
H
vertebrarterial canal
oblique foramen
I
J
K
L
M
N
O
P
Q
R
S
T
V
CaXVII
U
CaXVI
CaXVII
CaXVI

Figure 22

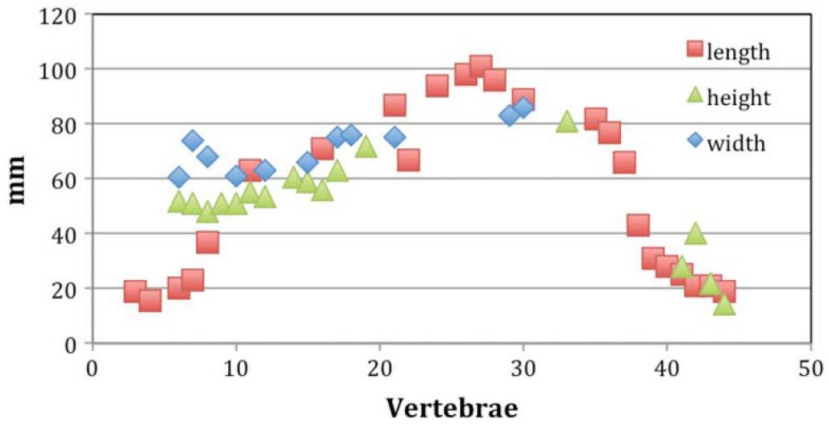
120
100
80
60
40
20
0
mm
0
10
20
30
40
50
Vertebrae
length
height
width

Figure 23

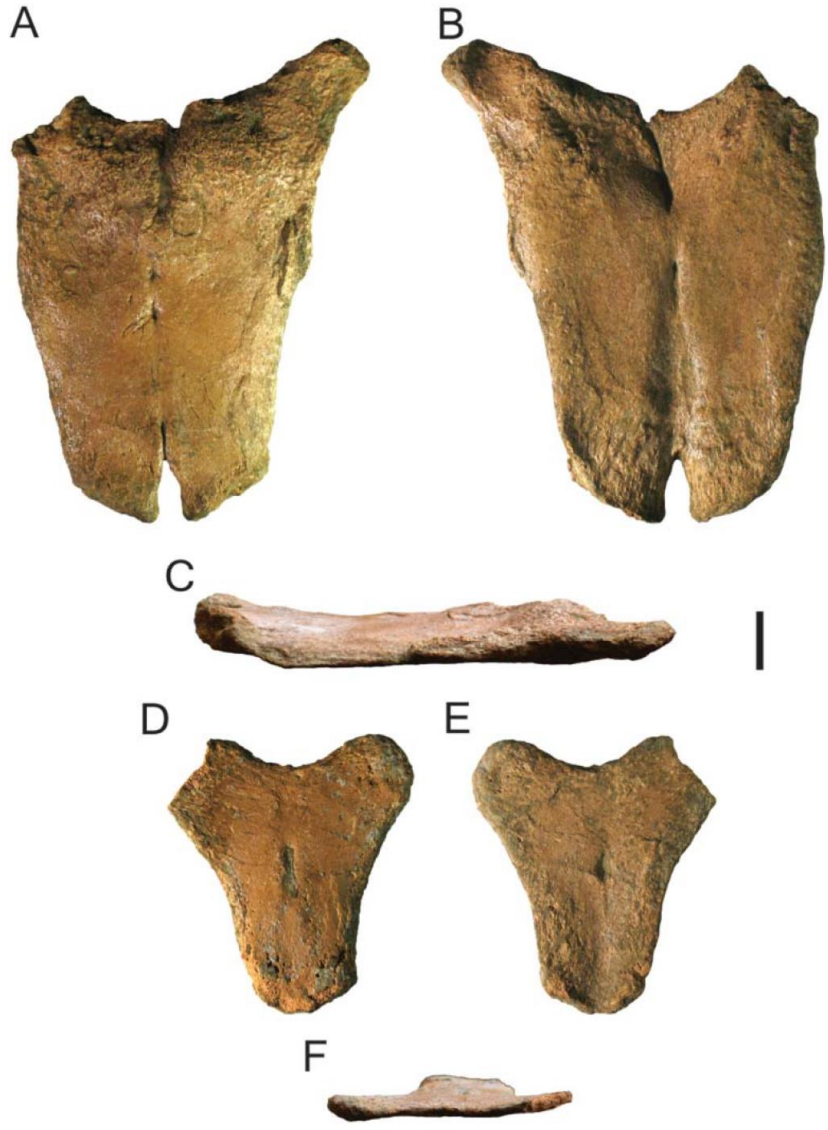

Figure 24

Figure 25

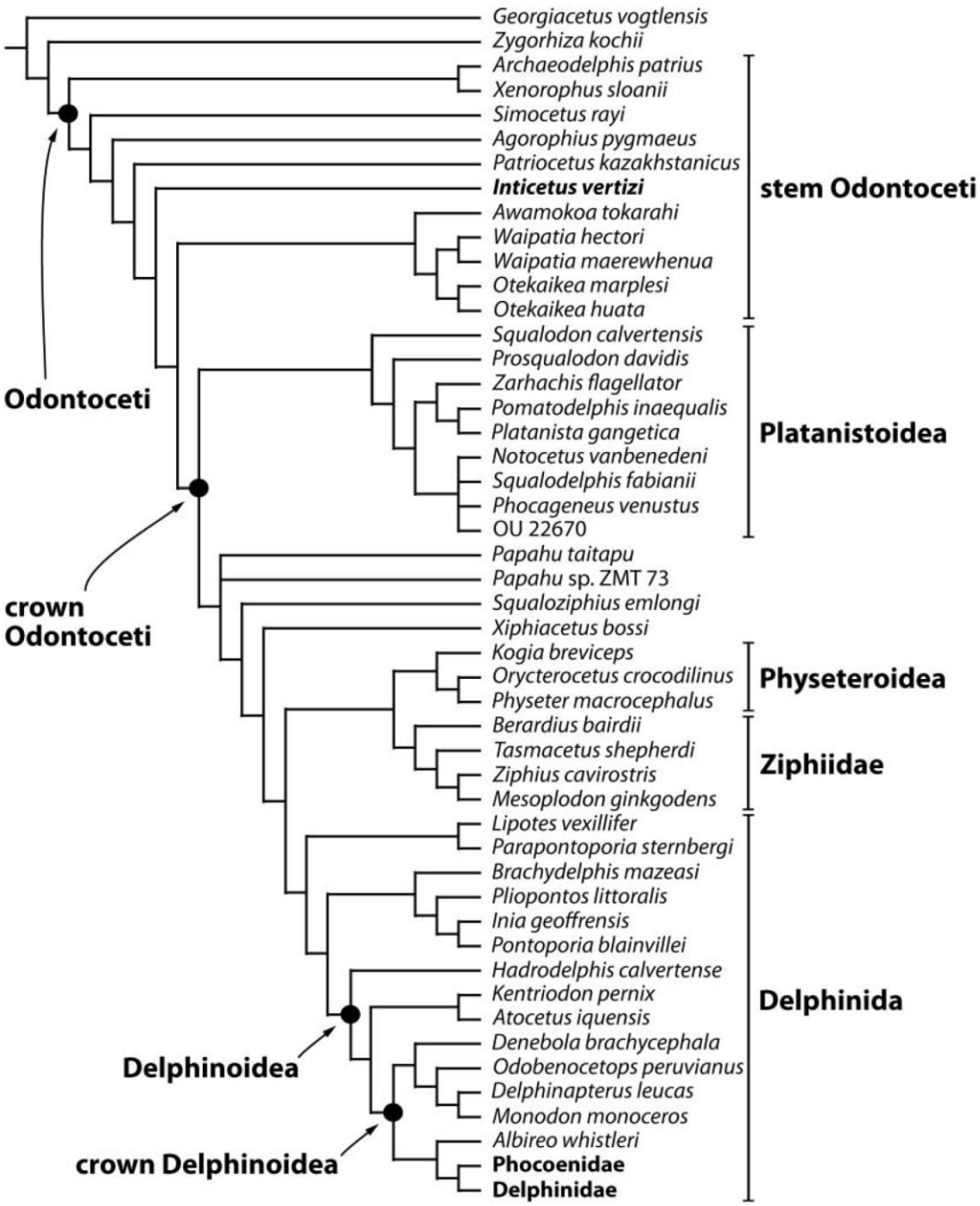
Georgiacetus vogtlensis
Zygorhiza kochii
Archaeodelphis patrius
Xenorophus sloanii
Simocetus rayi
Agorophius pygmaeus
Patriocetus kazakhstanicus
Inticetus vertizi
Awamokoa tokarahi
Waipatia hectori
Waipatia maerewhenua
Otekaikea marplesi
Otekaikea huata
stem Odontoceti
Squalodon calvertensis
Prosqualodon davidis
Zarhachis flagellator
Pomatodelphis inaequalis
Platanista gangetica
Notocetus vanbenedeni
Squalodelphis fabianii
Phocageneus venustus
OU 22670
Platanistoidea
Odontoceti
Papahu taitapu
Papahu sp. ZMT 73
Squaloziphius emlongi
Xiphiacetus bossi
crown Odontoceti
Kogia breviceps
Orycterocetus crocodilinus
Physeter macrocephalus
Physeteroidea
Berardius bairdii
Tasmacetus shepherdi
Ziphius cavirostris
Mesoplodon ginkgodens
Ziphiidae
Lipotes vexillifer
Parapontoporia sternbergi
Brachydelphis mazeasi
Pliopontos littoralis
Inia geoffrensis
Pontoporia blainvillei
Hadrodelphis calvertense
Kentriodon pernix
Atocetus iquensis
Denebola brachycephala
Odobenocetops peruvianus
Delphinapterus leucas
Monodon monoceros
Albireo whistleri
Phocoenidae
Delphinidae
Delphinida
Delphinoidea
crown Delphinoidea

Figure 26

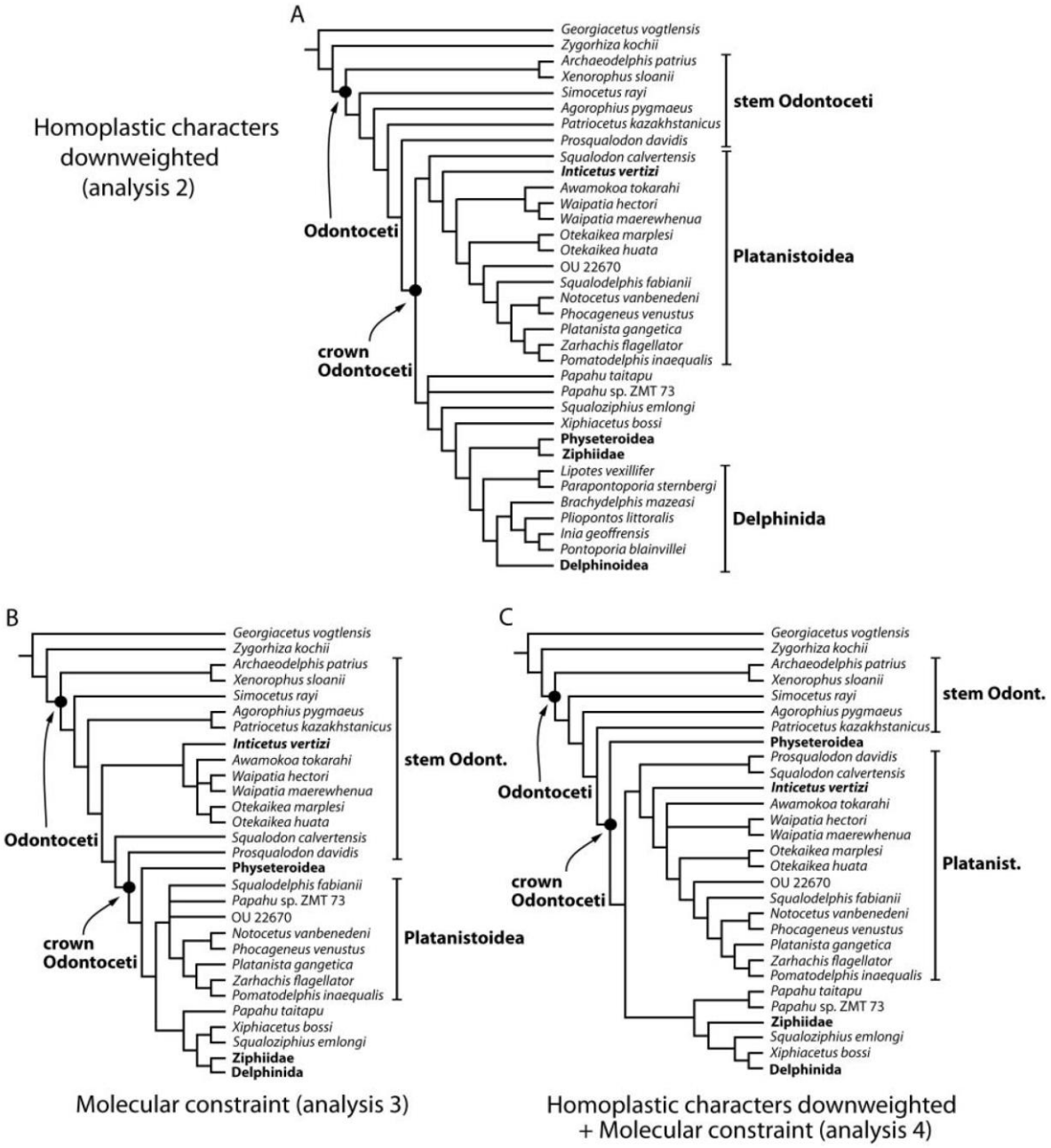
A
Homoplastic characters downweighted (analysis 2)
Georgiacetus vogtlensis
Zygorhiza kochii
Archaeodelphis patrius
Xenorophus sloanii
Simocetus rayi
Agorophius pygmaeus
Patriocetus kazakhstanicus
Prosqualodon davidis
Squalodon calvertensis
Inticetus vertizi
Awamokoa tokarahi
Waipatia hectori
Waipatia maerewhenua
Otekaikea marplesi
Otekaikea huata
OU 22670
Squalodelphis fabianii
Notocetus vanbenedeni
Phocageneus venustus
Platanista gangetica
Zarhachis flagellator
Pomatodelphis inaequalis
Papahu taitapu
Papahu sp. ZMT 73
Squaloziphius emlongi
Xiphiacetus bossi
Physeteroidea
Ziphiidae
Lipotes vexillifer
Parapontoporia sternbergi
Brachydelphis mazeasi
Pliopontos littoralis
Inia geoffrensis
Pontoporia blainvillei
Delphinoidea
stem Odontoceti
Platanistoidea
Delphinida
Odontoceti
crown Odontoceti
B
Molecular constraint (analysis 3)
stem Odont.
Platanistoidea
Delphinida
C
Homoplastic characters downweighted + Molecular constraint (analysis 4)
stem Odont.
Platanist.

Figure 27

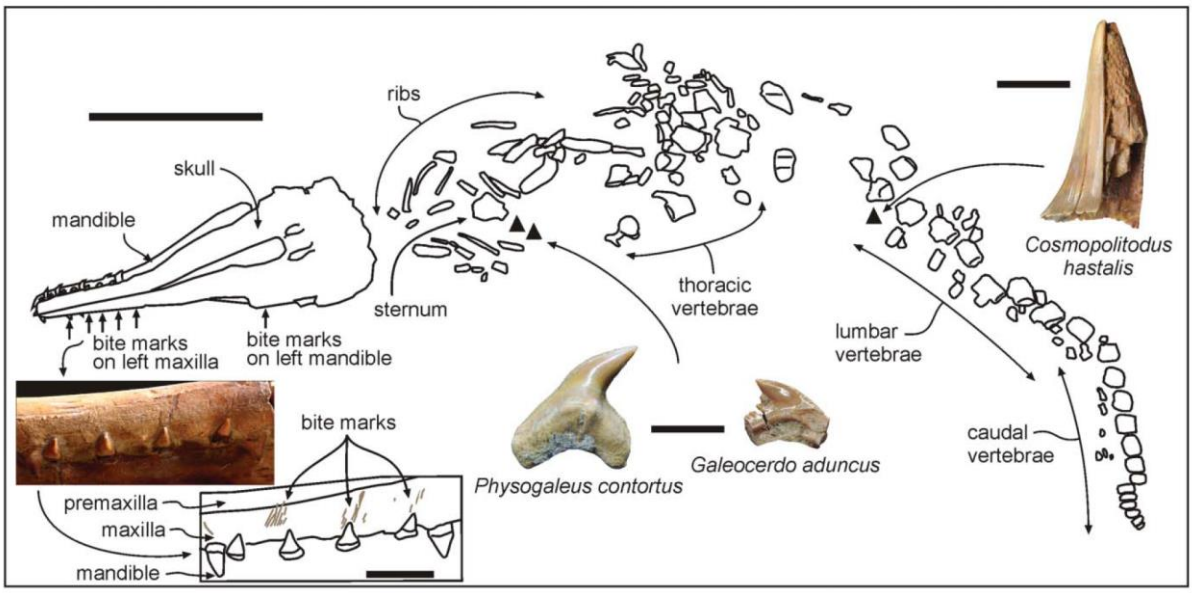
ribs
skull
mandible
sternum
thoracic vertebrae
lumbar vertebrae
caudal vertebrae
bite marks on left maxilla
bite marks on left mandible
bite marks
premaxilla
maxilla
mandible
Physogaleus contortus
Galeocerdo aduncus
Cosmopolitodus hastalis

Figure 28